Diffuse Dust in Elliptical Galaxies

by

Jonathan Savoy

A Thesis Submitted to
Saint Mary's University, Halifax, Nova Scotia
in Partial Fulfillment of the Requirements for the Degree of

MASTER OF SCIENCE

in

Astronomy

(Department of Physics and Astronomy)

September 26, 2007, Halifax, Nova Scotia

Approved: Gary A. Welch
Supervisor

Approved: Marcin Sawicki
Examiner

Approved: David G. Turner
Examiner

Date: September 26, 2007

Your file Votre référence
ISBN: 978-0-494-35775-0
Our file Notre référence
ISBN: 978-0-494-35775-0

Abstract

Diffuse Dust in Elliptical Galaxies, by *Jonathan Savoy*, submitted on September 26, 2007:

It is well established that the broadband colors of elliptical galaxies become redder near their centres, which provides an important constraint on models of elliptical galaxy formation. The observed radial color gradients are usually explained by a gradient in stellar metallicity, but if a diffuse dust component were present, it could also contribute to the reddening. Dust clouds are commonly observed near the centres of elliptical galaxies, but the dust mass implied from optical extinction is generally 5-10 times less than values derived from far infrared (FIR) emission measured by *IRAS* photometry. One explanation for this discrepancy is that the majority of the dust is diffusely distributed, and not concentrated in dense clouds, but previous FIR experiments have lacked the spatial resolution to determine the location of the existing dust. In an effort to determine the importance of a diffuse dust component, 23 elliptical galaxies have been observed with the SCUBA instrument on the *JCMT*. The observations, combined with published fluxes, are modeled using a three dimensional Monte Carlo radiation transfer code to establish the mass, temperature, and distribution of diffuse dust in elliptical galaxies. The implied dust masses are often an order of magnitude larger than *IRAS* estimates, and the impact on the observed colour gradients is found to be negligible.

Acknowledgements

Gary: Thanks for the enormous amount of help you've given me over the last few years. It is a pleasure to work with you, and I think we make a great team.

Marcin and Dave Turner: Thanks for all the helpful comments and suggestions.

Mom and Dad: Thank you for all your love and support. Your regular Sunday and Wednesday phone calls were a soothing constant over the last six years (the homemade bread supply didn't hurt, either).

Beth: This project, as with most things I've done, would not have been possible without you. You are always there to pick me up, and I still don't know how everyone else manages. Because of you, the future looks wonderful.

Contents

List of Figures

List of Tables

Chapter 1

Introduction

The origins of early-type galaxies, which include elliptical (E) and lenticular (S0) galaxies, remain unclear. The proposed formation scenarios include the hierarchical buildup of galaxies through merging, or the monolithic collapse of isolated, overdense regions at high redshift. Helping to identify the most likely scenario for elliptical galaxy formation and evolution through studies of their current interstellar medium (ISM), encompasses the broad motivation behind this study.

Although the ISM in elliptical galaxies is difficult to detect at optical wavelengths, recent observations at a range of other wavelengths have revealed the presence of all phases of the ISM. Hot gas ($\sim 10^7$ K) is detected in diffuse X-ray emission (Forman *et al.*, 1985), while warm gas ($\sim 10^4$ K) is observed through line emission in around 55% of ellipticals (Kim, 1989). Molecular gas is detected in the form of CO (Wiklind *et al.*, 1995), and significant amounts of H I are sometimes observed (Knapp *et al.*, 1985). Dust should also be present in elliptical galaxies, since it is returned to the ISM as a product of stellar evolution. Indeed, dust is commonly seen in absorption features near the centres of ellipticals in deep optical images (Lauer *et al.*, 2005), and far-infrared (FIR) emission from cold ($\sim$25 K) dust is detected in $\sim$50% of galaxies observed with the *Infrared Astronomical Satellite*, *IRAS* (Knapp *et al.*, 1989). Curiously, the dust mass implied by *IRAS* observations at 60 and 100 μm is generally 5-10 times

greater than the amount estimated to be present in optical dust lanes and patches (Goudfrooij & de Jong, 1995). One explanation for this discrepancy is that the majority of the dust is diffusely distributed throughout the galaxy, and not contained in dense clouds, but previous FIR experiments have lacked the spatial resolution to determine the location of the existing dust.

Further evidence for a cool, diffuse dust component in elliptical galaxies has come from observations with the *Infrared Space Observatory, ISO* (Temi *et al.*, 2004), which can observe cooler dust at wavelengths out to 200 μm. Temi *et al.* (2004) report that *ISO* observations imply dust masses that are often more than 10 times greater than those inferred from *IRAS* observations alone. The addition of observations at wavelengths longer than 100 μm also means that the FIR spectral energy distribution (SED) of most elliptical galaxies cannot be well fit with a single temperature dust model. This emphasises the need for additional long-wavelength observations and a more thorough modelling process to establish the mass and temperature of dust in elliptical galaxies.

A diffuse dust component could have a substantial impact on the interpretation of broadband colour measurements of elliptical galaxies. It is well established that ellipticals generally become redder near their centres, which provides an important constraint on models of elliptical galaxy formation and evolution (La Barbera *et al.*, 2005). The observed radial colour gradients are usually explained by a gradient in stellar metallicity (Carollo *et al.*, 1993; Kobayashi & Arimoto, 1999) and age, but if a diffuse dust component were present, it could also contribute to the reddening (Wise & Silva, 1996; Witt *et al.*, 1992). Wise & Silva (1996) even suggest that for

many galaxies, the observed colour gradients can be reproduced entirely with dust masses that are comparable to those inferred by *IRAS* observations. Since metallicity gradients are observed in many early-type galaxies, dust is not believed to be the only source of colour gradients, but the findings of Wise & Silva (1996) imply that the effects of dust could be large.

Metallicity gradients can be traced using photospheric line strengths (Carollo *et al.*, 1993; Kobayashi & Arimoto, 1999), but this technique has been applied to only a relatively small sample of elliptical galaxies and is limited to the central regions (about half the effective radius) by the rapid decrease of surface brightness with radius. Optical colour gradients, on the other hand, can be more easily obtained for distant systems, and can be traced to larger galactic radii (Peletier *et al.*, 1990; Wu *et al.*, 2005). Because of these advantages, measuring radial colour gradients will continue to be a valuable technique for tracing the underlying stellar populations of early-type galaxies.

It is important to establish the potential impact of diffuse dust on radial colour gradients (and the inferred metallicity gradients) because they can be used to discriminate between various formation scenarios for early-type galaxies. In the monolithic formation scenario, early-type galaxies are formed at high redshift through the rapid collapse of dense regions, and metallicity gradients are expected to be produced as galactic winds remove gas at large radii more effectively than in the central regions. Monolithic models predict large metallicity gradients that often exceed those that have been observed (Carlberg, 1984). In simulations of hierarchical, merger-driven galaxy formation, the mixing of stellar populations can lower the predicted metallicity

gradients to values that are consistent with the observed range (Kobayashi, 2004). If a diffuse dust component were present, it could contribute to the observed reddening and reduce the inferred metallicity gradients, which would support the role of major mergers in early-type galaxy formation (Wu *et al.*, 2005). Any model of elliptical galaxy formation must account for the observed colour gradients, but it is impossible to determine the impact of dust on these measurements without knowing the location and amount of dust present.

The SCUBA instrument on the *James Clerk Maxwell Telescope* (*JCMT*) was the first of a new generation of ground-based detectors capable of producing images and total flux measurements of the sub-mm radiation of diffuse interstellar dust heated to temperatures of 20-30 K by starlight. In an effort to study the cold dust in early type galaxies, several programs obtained SCUBA observations at 450 and 850 μm. It is worth noting that the predicted 450 and 850 μm flux densities based on the *IRAS* observations of the SCUBA sample are typically $\sim$100 mJy and $\sim$10 mJy, respectively. For the SCUBA exposure times considered here, clear detections are only expected in a few cases, with most observations providing useful upper limits on the amount of dust in each galaxy.

The goals of this study are to establish the mass, temperature, and distribution of diffuse dust in a sample of elliptical galaxies and to assess the impact that it has on the observed radial colour gradients. The derived dust masses are then compared to the values expected from stellar evolution. The current project involves first carefully reducing a sample of 23 SCUBA observations of E and S0 galaxies in an attempt to obtain flux measurements and direct images of the existing dust. Combining these

observations with published fluxes through optical and FIR passbands results in a detailed SED of both the stellar content and the dust component. A three-dimensional Monte Carlo radiation transfer code supplied by Kenneth Wood that produces various synthetic passband fluxes and images is used to model the observations. An oblate Jaffe law (Jaffe, 1983; Capaccioli *et al.*, 1993), appropriate to the three-dimensional structure of ellipticals, is used to define separately the density distribution of both the starlight and dust. Additional dust distributions are also explored. Input parameters for the models include the total stellar luminosity (which depends on the assumed distance of the galaxy), observed filter fluxes, total dust mass, and the ellipticity and scale lengths of the Jaffe distributions.

Each galaxy is individually modeled by fitting the predicted SED to the available data and then analyzing the resulting synthetic images. This process constrains the amount and distribution of diffuse dust in each galaxy. Because of the time required to compute each model, the SEDs are fit by eye, which introduces an uncertainty of 5-10% in the dust mass determination. Once a model has been fit to the observations, the colour gradient produced by the dust can be directly measured from the synthetic optical images. This procedure quantifies the impact of diffuse dust on radial colour gradients measured in elliptical galaxies on an individual basis, which could provide valuable insights on the currently proposed formation scenarios.

Chapter 2

Galaxy Sample and SCUBA Observations

The most complete catalogue of FIR data for elliptical galaxies is still the *IRAS* sample of Knapp *et al.* (1989), in which about half of the galaxies were detected above the 3σ level at 60 and 100 μm. Later, Bregman *et al.* (1998) carefully re-reduced the data for a subset of early-type galaxies without active galactic nuclei (AGN) that appeared normal, and found that only 17% of the sample was detected above a 90% confidence level. Most of the galaxies selected for SCUBA observations were normal elliptical galaxies with well-determined *IRAS* fluxes from the Bregman *et al.* (1998) sample. The complete sample of galaxies observed with SCUBA can be found in Table 2.1. The SCUBA observations come from four observing programs between 1997 and 1999 (M96BC47/8, M98AC32, M99AC05, M99BC07), supplemented with archival observations of elliptical galaxies (including data from programs M97AN14, M97BH02, M98BC25). A summary of the observations can be found in Table 2.2.

In order to search for spatially extended dust emission, SCUBA observations of the galaxy centres were obtained at 450 and 850 μm in jiggle-map mode. In this process, the secondary mirror is 'jiggled' in a 64-point pattern with 3-arcsecond spacing to fully sample the sky at 450 μm. The 450 μm array is composed of 91 bolometers arranged in five concentric hexagonal rings around a central detector; the 850 μm

Galaxy	Type	D (Mpc)	$\log(L_{B,\odot})$	Axial Ratio	R_{Jaffe} (pc)
NGC 1339	-4.2 ± 0.5	14.6	9.24	0.72	1600
NGC 1400	-3.7 ± 1	5	8.64	0.87	931
NGC 1531	-2.5 ± 1.5	13	9.01	0.69	
NGC 2693	-4.8 ± 0.5	73.1	10.57	0.69	9420
NGC 2974	-4.7 ± 0.8	21.5	9.95	0.59	3330
NGC 3156	-2.4 ± 1.1	22.4	9.44	0.58	2040
NGC 3265	-4.8 ± 0.4	22.4	9.12	0.78	483
NGC 3377	-4.8 ± 0.5	11.3	9.62	0.58	2480
NGC 3379	-4.8 ± 0.5	11.1	9.95	0.89	2490
NGC 3872	-4.8 ± 0.4	45.1	10.23	0.63	5180
NGC 4061	-4.9 ± 0.6	14.6	8.82	0.76	
NGC 4261	-4.8 ± 0.4	31.6	10.40	0.89	7240
NGC 4278	-4.8 ± 0.4	14.9	9.89	0.93	3260
NGC 4283	-4.8 ± 0.6	15.7	9.14	0.98	1250
NGC 4308	-4.7 ± 0.8	9.7	8.27	0.89	
NGC 4494	-4.8 ± 0.4	17.1	10.14	0.74	5290
NGC 4697	-4.8 ± 0.5	11.7	10.04	0.65	5350
NGC 4786	-4.2 ± 0.6	66.4	10.55	0.78	7290
NGC 5353	-2.1 ± 0.6	37.8	10.29	0.50	3530
NGC 6524	-2.8 ± 1.2	76.9	10.28	0.72	10700
NGC 6702	-4.8 ± 0.5	50.4	10.23	0.72	
UGC 7354	-4.7 ± 1.7	14.6	8.60	0.85	1460
UGCA 298	-3.3 ± 1.3			0.69	

Table 2.1: Properties of the galaxy sample observed with SCUBA. The numerical type and the corrected B-band magnitudes used to calculate the luminosity are from the online HyperLeda catalogue. For reference, -5 indicates a pure elliptical and -2 signifies a pure S0. The axial ratio and the effective radii used to calculate the Jaffe radii (Equation 4.3) are from the Third Reference Catalogue of Bright Galaxies (de Vaucouleurs *et al.*, 1991). In order of preference, the distances are from: surface brightness fluctuation measurements from the NASA/IPAC Extragalactic Database (NED) distance compilation, the Nearby Galaxies Catalogue (Tully, 1988), or the Hubble flow distance.

Galaxy	Integrations	Date	Calibrators	FCF
NGC 1339	16	3/26/1998	irc+10216,crl618	1.04, 1.03
	16	3/27/1998	irc+10216,crl618	0.98, 0.98
NGC 1400	24	12/21/1997*	Crl618	1.08
NGC 1531	32	3/27/1998	irc+10216,crl618	0.98, 0.98
NGC 2693	20	11/19/1999	Crl618	1.21
NGC 2974	75	6/16/1997		1.05
	120	6/17/1997		1.05
	20	11/19/1999	Crl618	1.21
	20	12/23/1997*	OH231.8	1.17
	25	1/22/1998*	Irc+10216	1.16
NGC 3156	20	11/19/1999	Crl618	1.21
NGC 3265	15	10/18/1997		1.05
	8	10/19/1997		1.05
NGC 3377	16	3/26/1998	irc+10216,crl618	1.04, 1.03
NGC 3379	32	3/27/1998	irc+10216,crl618	0.98, 0.98
NGC 3872	20	11/19/1999	Crl618	1.21
NGC 4061	16	3/26/1998	irc+10216,crl618	1.04, 1.03
NGC 4261	120	12/1/1997*		0.86
NGC 4278	150	6/16/1997		1.05
	180	6/17/1997		1.05
	8	3/26/1998	irc+10216,crl618	1.04, 1.03
	16	3/27/1998	irc+10216,crl618	0.98, 0.98
NGC 4283	16	3/26/1998	irc+10216,crl618	1.04, 1.03
NGC 4308	16	3/26/1998	irc+10216,crl618	1.04, 1.03
NGC 4494	16	3/27/1998	irc+10216,crl618	0.98, 0.98
NGC 4697	20	11/20/1999	Uranus	1.14
NGC 4786	20	11/19/1999	Crl618	1.21
NGC 5353	20	11/19/1999	Crl618	1.21
	80	11/20/1999	Uranus	1.14
NGC 6702	45	8/6/1997*	Uranus	1.02
NGC 6524	150	6/16/1997		1.05
	135	6/17/1997		1.05
	100	4/18/1999	Mars,Uranus	1.07, 1.07
	30	4/19/1999	Mars	1.08
	15	8/14/1998*	Mars	1.28
UGC 7354	32	3/26/1998	irc+10216,crl618	1.04, 1.03
UGCA 298	24	3/27/1998	irc+10216,crl618	0.98, 0.98

Table 2.2: Summary of the SCUBA observations reduced in the current study. An asterisk indicates data that were not from the four primary observing programs. The Flux Calibration Factors are calculated for a 40″ aperture, and have units of Jy arcsec^{-2} Volt^{-1}. If no calibrators were available, the FCFs from Jenness *et al.* (2002) were used.

array has 37 detectors in three hexagonal rings around the central detector. Since the FWHM (full width at half maximum) of the 450 μm beam is about 7″ and that of the 850 μm beam is about 15″, the 850 μm map is oversampled in standard jiggle mode. To remove atmospheric emission, chopping is performed at each jiggle position, where the secondary 'chops' the array at a rate of 7.8 Hz to a reference position about 100″ away in azimuth. An integration, defined as a complete 64-point sampling of the source, takes about 128 seconds to complete, and several (10-20) integrations are grouped together into a single data file containing both the 850 and 450 μm observations. To improve atmospheric subtraction, each integration is split into four 16-point 'exposures', in between which the telescope 'nods' in the opposite direction of the chop throw, switching the position of the source and the chop location. The total field of view is about 2.3 arcminutes in diameter at both 450 and 850 μm.

2.1 Data Reduction

Details of the SCUBA data reduction process carried out with SURF (SCUBA User Reduction Facility) can be found in Appendix A. The reduction process results in maps that have units of Volts. The important step of converting the instrumental output into a measure of flux requires observations of standard sources of known brightness.

To calibrate the data, the standard sources listed in Table 2.1 were observed. The planets Mars, Uranus, and Neptune are the primary calibrators for SCUBA; all other standard sources used in this study are secondary calibrators. In order to obtain

integrated fluxes, the calibration was carried out in terms of flux per square arcsecond within a 40″ diameter aperture, instead of flux per beam area (Jenness *et al.*, 2002). This means that the measured flux for both the calibrator and the observed galaxies on each night is that within a 40″ aperture. To convert the measured voltages to flux densities, the flux calibration factor (FCF) can be calculated for each standard source with the following relationship in $Jyarcsec^{-2}Volt^{-1}$:

$$FCF_{int} = \frac{S_{tot}}{V_{int}A}, \tag{2.1}$$

where S_{tot} is the total expected flux within the aperture, V_{int} is the measured voltage from the image, and A is the area of the aperture used. The online program *FLUXES* was used to predict the planetary fluxes at the time of the observations, and the secondary calibrator fluxes were taken from the SCUBA calibration website. From the FCFs listed in Table 2.2, the measured voltages were converted to flux densities in Jy for individual nights.

Chapter 3

SCUBA Images and Flux Densities

The SCUBA images of the detected galaxies are presented in Figures 3.1 and 3.2. The observed fluxes and upper limits are found in Table 3.1. The reported fluxes are for a 40″ diameter aperture centred on the optical position of each galaxy, taken from the NASA/IPAC Extragalactic Database (NED). The fluxes were found using KAPPA's (Kernel Application Package) APERADD command. The uncertainty reported in each measurement is the standard deviation of five or more independent 40″ aperture samples of the image outside of the central 40″. The upper limits for non-detections correspond to σ standard deviations. The placement and measurement of the independent apertures was carried out with GAIA (Graphical Astronomy and Image Analysis Tool). Detections are cases where the aperture flux exceeds three times the standard deviations.

The uncertainties quoted in Table 3.1 refer only to the statistical uncertainties present in the final images. There are several other sources of uncertainty in the measured fluxes that should be mentioned. One source of uncertainty is the opacity value used to correct for atmospheric attenuation. As discussed in Appendix A, the most reliable estimate of the sky opacity comes from the nearby CSO Tau monitor, which samples the sky every ten minutes at a frequency of 225 GHz. The measured extinction values often vary by 10-20% between samples, and additional uncertainty

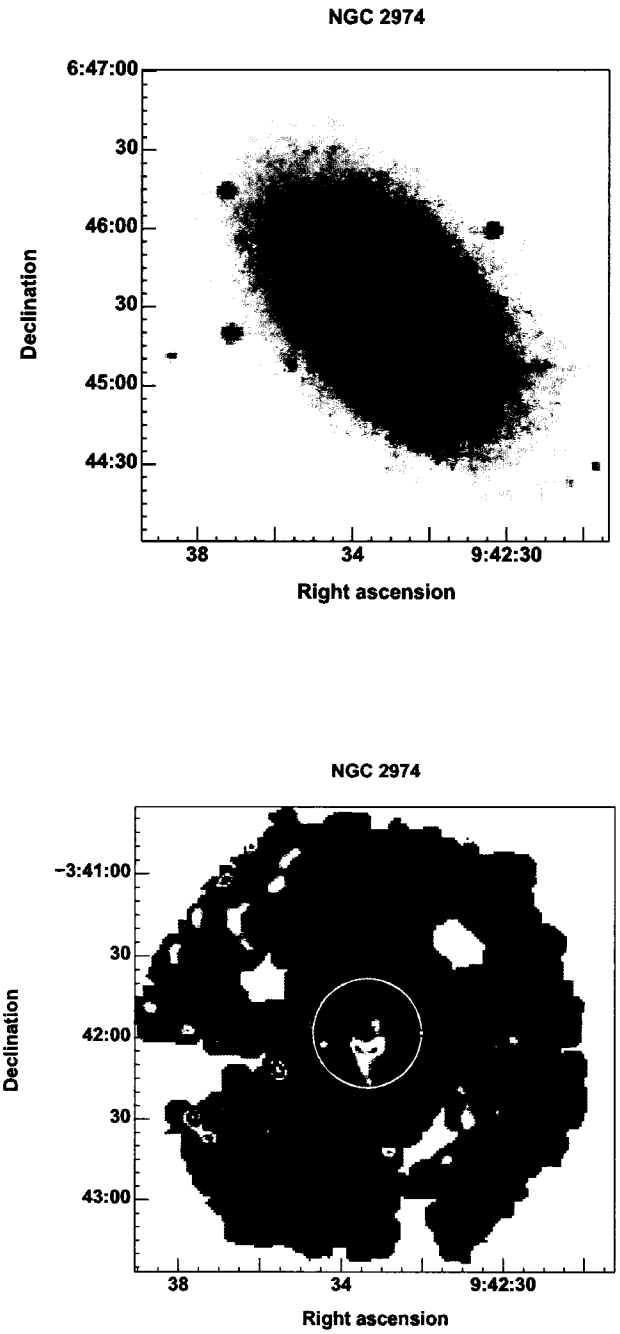

Figure 3.1: a.) $3 \times 3'$ Digitized Sky Survey (DSS) images taken from the NED, and SCUBA 850 μm images of the detected galaxies. The circle in each SCUBA image represents the $40''$ diameter aperture used to calculate the flux densities listed in Table 3.1. It is centred on the optical position of the galaxy taken from the NED. There is an error in the declination coordinate for the DSS image of NGC 2974.

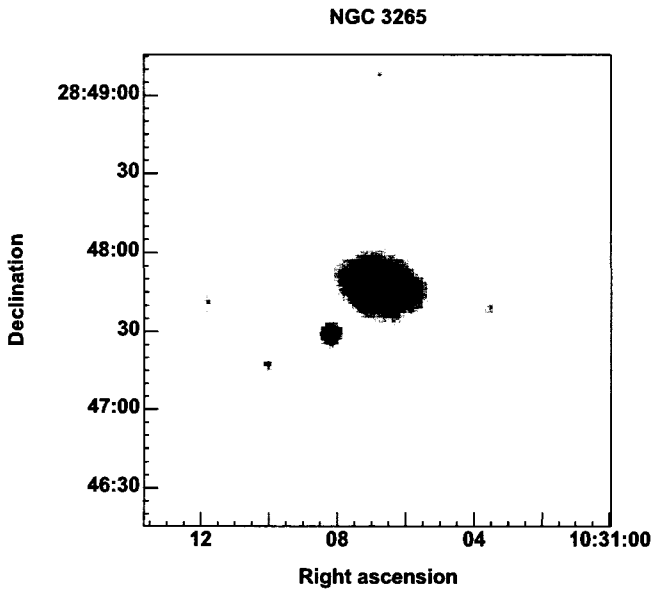

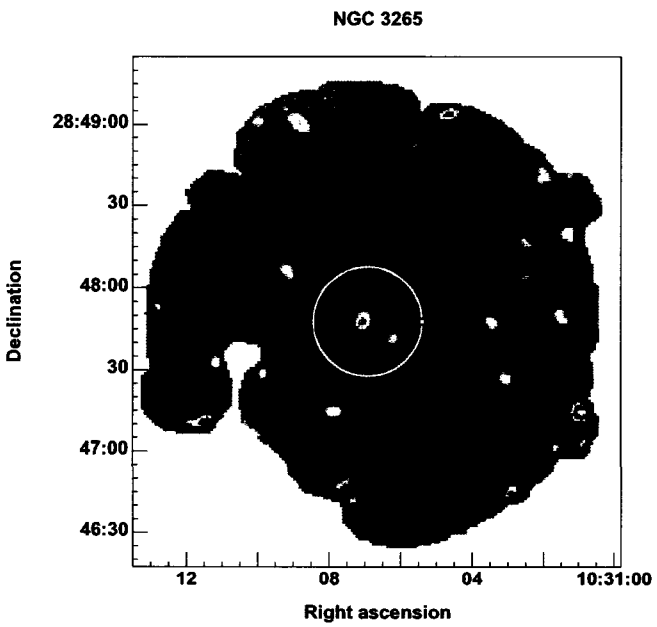

Figure 3.1: b.) (*cont'd*) SCUBA 850 μm images.

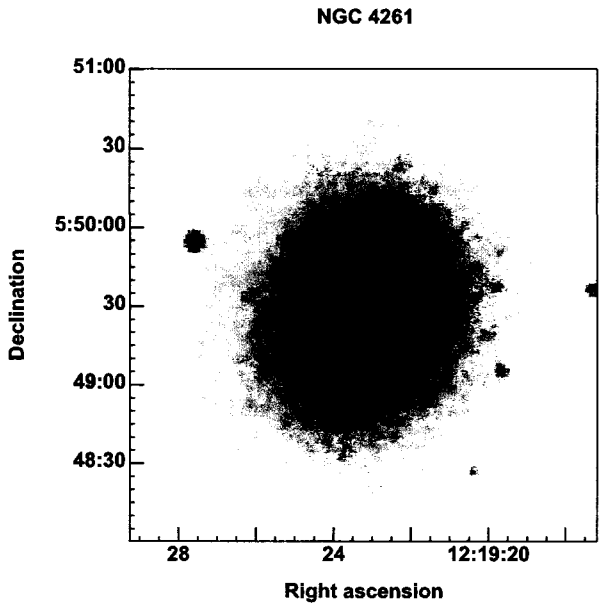

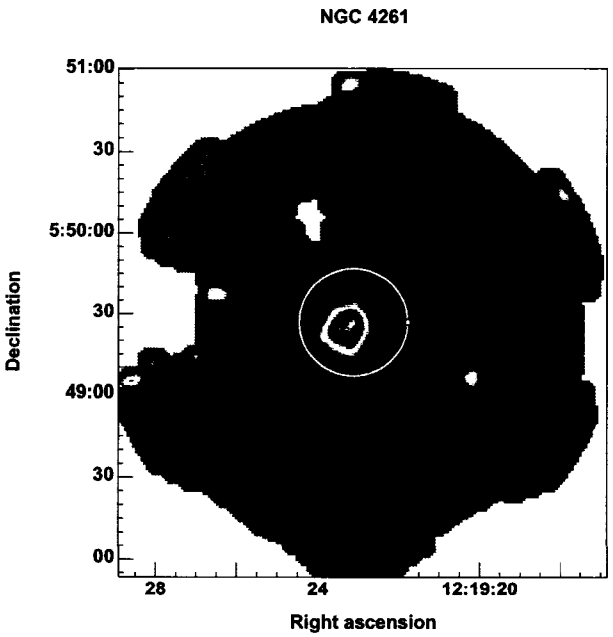

Figure 3.1: c.) (*cont'd*) SCUBA 850 μm images.

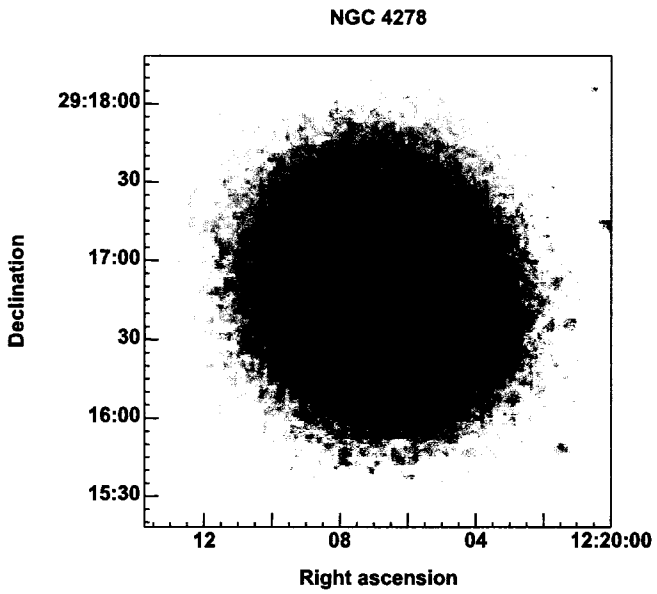

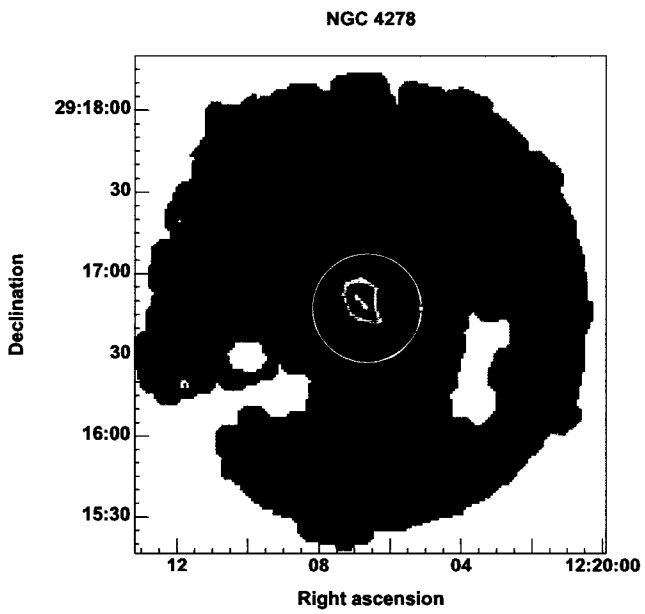

Figure 3.1: d.) (*cont'd*) SCUBA 850 μm images.

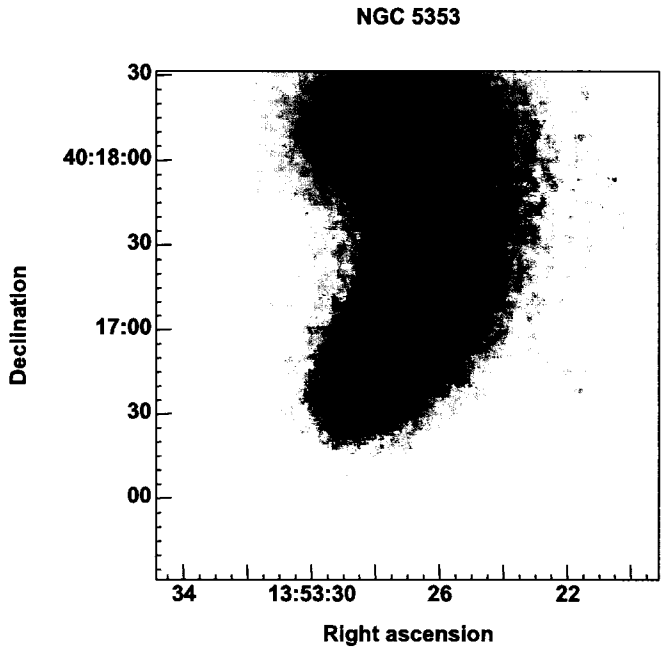

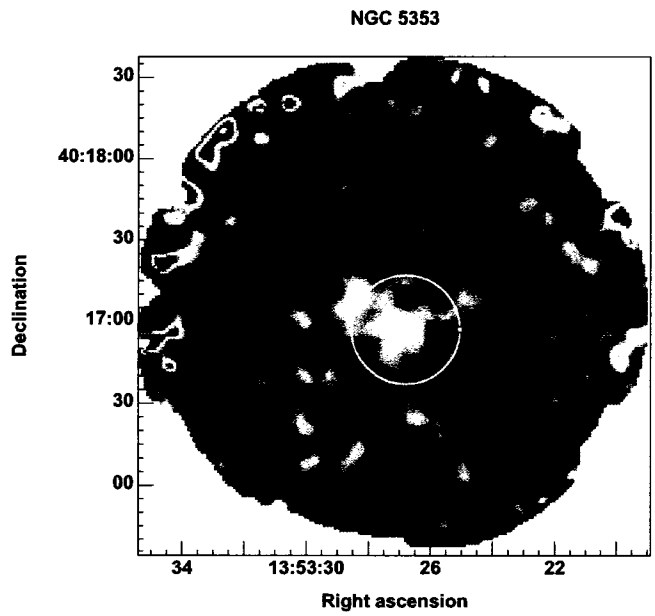

Figure 3.1: e.) (*cont'd*) SCUBA 850 μm images.

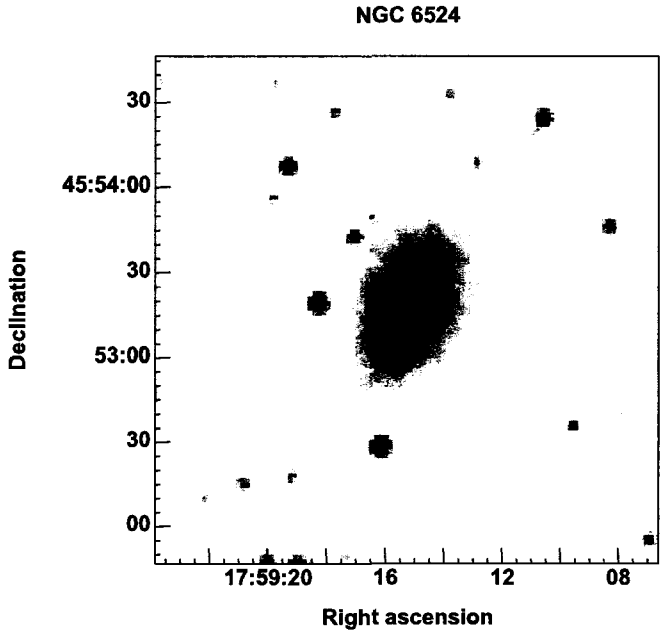

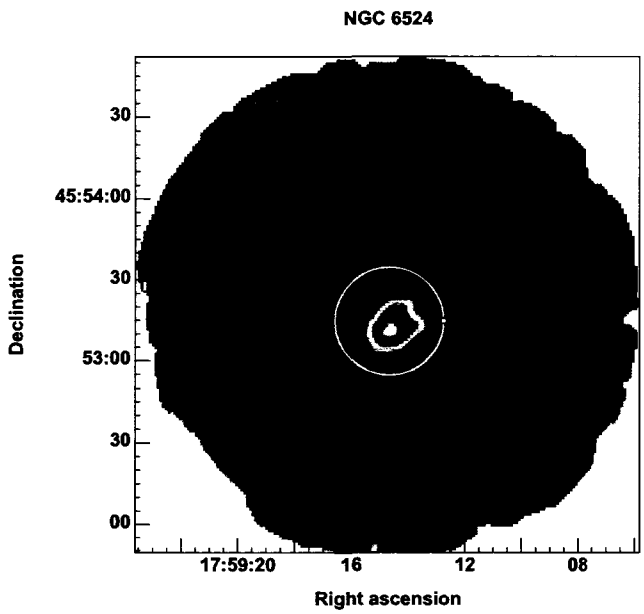

Figure 3.1: f.) (*cont'd*) SCUBA 850 μm images.

Galaxy	F_{850} (mJy)	F_{450} (mJy)	F_{100} (mJy)	F_{60} (mJy)
NGC 2974	19 ± 5.6	< 200	1420 ± 80	420 ± 33
NGC 3265	34 ± 7.8	< 160	4150 ± 79	2520 ± 29
NGC 4261	180 ± 17.0		150 ± 49	80 ± 35
NGC 4278	48 ± 8.5	< 73	1960 ± 111	660 ± 49
NGC 5353	48 ± 9.6	< 320	1270 ± 111	340 ± 88
NGC 6524	70 ± 3.9	356 ± 73	8890 ± 82	3750 ± 21
NGC 1339	< 8.7	< 160	670 ± 58	230
NGC 1400	< 9.5	< 40	3280 ± 146	740 ± 39
NGC 1531	< 9.2	< 180		
NGC 2693	< 16.0	< 120	900 ± 117	230 ± 49
NGC 3156	< 11.0	< 70	910 ± 95	220 ± 37
NGC 3377	< 7.9	< 100	850 ± 124	140 ± 47
NGC 3379	< 11.0	< 120	< 109	< 41
NGC 3872	< 9.8	< 180	750 ± 106	120 ± 55
NGC 4061	< 8.3	< 59		
NGC 4283	< 8.0	< 42	< 78	< 34
NGC 4308	< 6.4	< 58	< 158	< 33
NGC 4494	< 6.5	< 66	<170	190 ± 49
NGC 4697	< 18.0		1590 ± 156	590 ± 53
NGC 4786	< 12.0	< 490	1310 ± 126	370 ± 36
NGC 6702	< 5.4		2680	< 47
UGC 7354	< 10.0	< 73	940 ± 94	730 ± 31
UGCA 298	< 4.7	< 58	< 621	500 ± 45

Table 3.1: SCUBA 450 and 850 μm flux densities for a 40″ diameter aperture centered on the optical positions. *IRAS* 60 and 100 μm flux densities are from Bregman *et al.* (1998) if available, or from the NED, otherwise. Note that NGC 1400 is a possible detection at 850 μm (23 mJy or 2.4σ) and that the 850 μm flux of NGC 6524 could be underestimated by 30-40% (Figure 3.3).

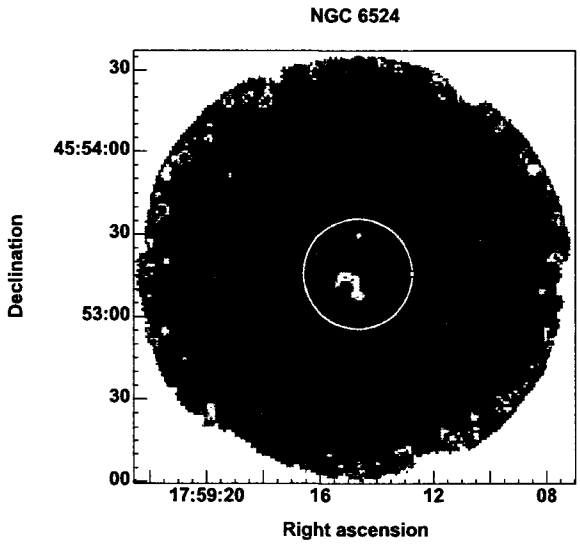

Figure 3.2: SCUBA 450 μm image of NGC 6524. The circle represents the 40″ diameter aperture used to calculate the flux density listed in Table 3.1.

is present in the scaling relations A.1 and A.2. The total uncertainty in flux density arising from extinction corrections is estimated to be $\leq$10%. Another uncertainty that was studied was in the removal of sky emission. The parallel reductions based on different methods of 'sky' bolometer selection, described in Appendix A, indicates small uncertainties arising from sky subtraction: the average uncertainty in flux attributable to sky bolometer selection is 0.6 mJy at 850 μm, or $\leq$3% of the detected flux.

An additional source of uncertainty comes from the determination of the FCF for each night. On nights when two calibrators were observed, there was excellent ($\leq$ 1.5%) agreement between the two (see Table 2.2), which increases the level of confidence that can be placed on nights when only one calibrator was observed. However,

on a few nights when no calibration observations were available, the published historical values (Jenness *et al.*, 2002) were adopted, which vary by up to 20%, depending on the conditions. The lack of calibration observations results in greater uncertainty on those nights. The total uncertainty in the 850 μm detections is estimated to be ~25-30%

Since the *IRAS* beam certainly sampled the total flux from each galaxy at 60 and 100 μm, it is worth considering whether the 40″ aperture used for the SCUBA observations encloses the total flux. NGC 6524 is the only galaxy in the sample that shows any convincing evidence of extended emission compared to the 40″ aperture at 850 μm. Figure 3.3 shows that perhaps ~30-40% of the emission of NGC 6524 is not included in the 40″ aperture.[1] Because the *IRAS* and SCUBA observations both appear to sample the total flux, the two data sets can be reliably compared.

3.1 Emission from Additional Sources

Two mechanisms in addition to thermal dust emission may contribute to the signal in the 850 μm passband. The first is emission from the CO(3-2) rotational transition at 345 GHz. Of the galaxies detected at 850 μm, only NGC 6524 (Knapp & Rupen, 1996) and NGC 3265 (Gordon, 1991) were also detected in CO emission, while NGC 2974 and NGC 4278 have observed upper limits (Bregman *et al.*, 1992). The detections and upper limits were in the CO(2-1) transition and an assumed CO(3-2)/CO(2-1) ratio of 0.5 (Garcia-Burillo *et al.*, 1993; Hafok & Stutzki, 2003) was used to predict

[1]The 850 μm flux of NGC 6524 was appropriately corrected for the modelling process described below.

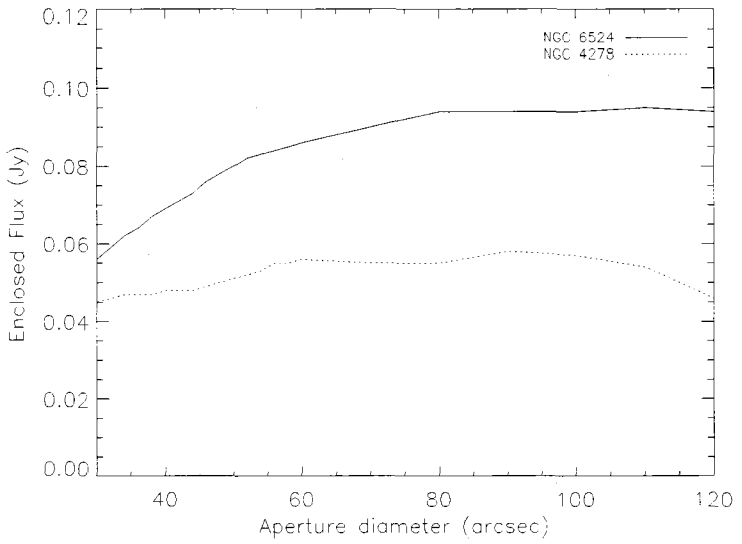

Figure 3.3: Enclosed 850 μm flux for varying aperture diameter for two well-detected galaxies. NGC 6524 shows evidence for extended emission beyond the 40″ diameter aperture used to calculate the flux densities listed in Table 3.1.

a CO(3-2) flux. The CO fluxes were then converted to 850 μm filter fluxes using the following:

$$F_{filter} = \frac{\int_0^\infty f_\lambda S_{850}\, d\lambda}{\int_0^\infty S_{850}\, d\lambda}, \tag{3.1}$$

where S_{850} is the transmission of the filter and f_λ is the line flux per unit wavelength interval. The resulting filter fluxes of 2.3 mJy for NGC 6524 and 2.6 mJy for NGC 3265 are less than the total uncertainties in the 850 μm fluxes. The upper limits for NGC 2974 and NGC 4278 result in filter fluxes of <0.75 and <0.90 mJy, respectively. Since the two detected galaxies are relatively gas-rich, it appears that the contribution of the CO(3-2) line to the SCUBA 850 μm fluxes is generally small in elliptical

galaxies. Nevertheless, the CO contribution was subtracted from the observed 850 μm flux during the modelling process described below.

The second possible contribution is from non-thermal emission produced by an AGN. The emission from an AGN peaks at much longer wavelengths, but a declining tail could produce a significant contribution to the 850 μm flux. The Photometry & SED database in the NED was searched to identify galaxies with an AGN. Figure 3.4 shows the radio data for 3 AGN in comparison to the *IRAS* and SCUBA values listed in Table 3.1, as well as *ISO* fluxes from Temi *et al.* (2004) at 60-200 μm.

In NGC 4261, all of the observed flux at 850 μm could be generated by AGN activity, while in NGC 4278 and NGC 5353 about half of the emission could be produced by an AGN. Since NGC 4278 is modeled in greater detail in Chapter 4, a more rigorous estimate of the AGN contribution has been made. Doi *et al.* (2005) report a flux of 0.403 Jy at 1.5 GHz, and suggest that a minimum likely slope for the non-thermal radio emission ($F_\lambda \sim \lambda^a$) is $a \geq 0.5$. Extrapolating down to 850 μm, a filter flux of 25.6 mJy is found for the SCUBA 850 μm passband from Equation 3.1. This contribution has been subtracted from the observed flux density of NGC 4278 when modelling the galaxy. From Figure 3.4, it should be noted that more of the SCUBA flux could be removed if a higher radio flux was chosen for the extrapolation.

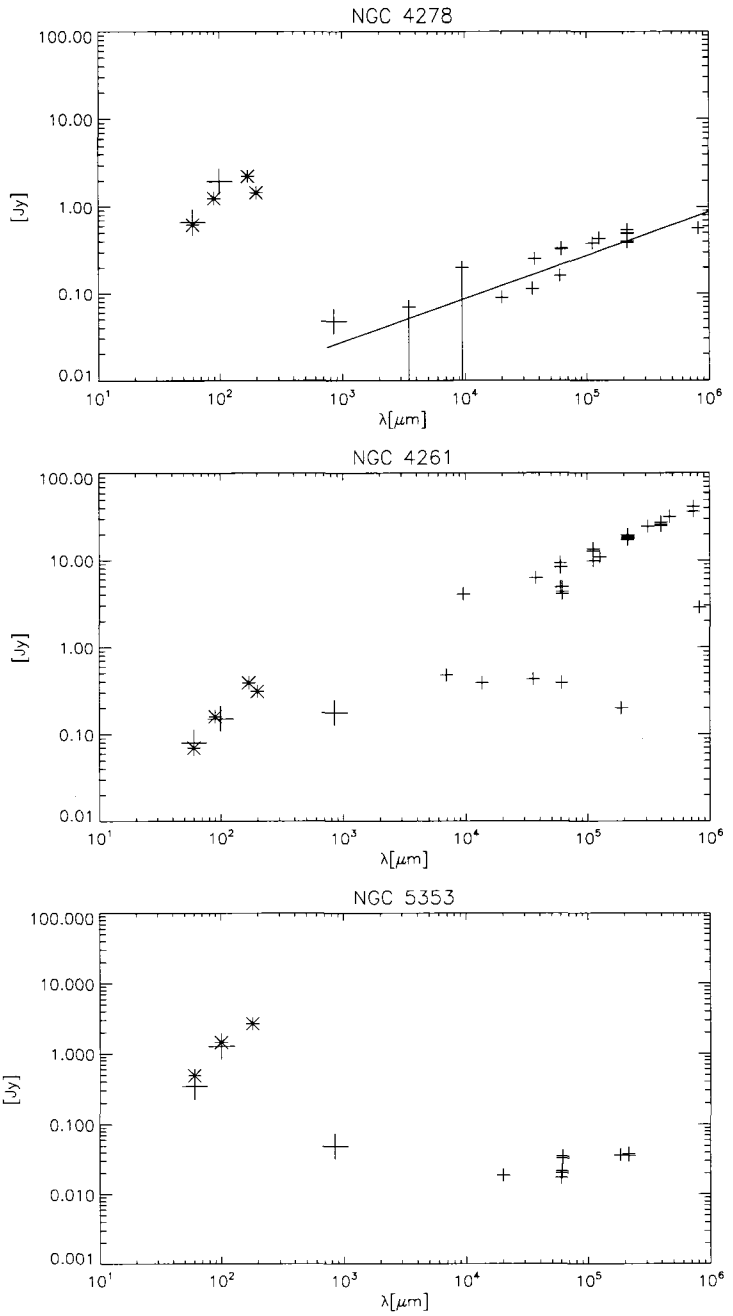

Figure 3.4: FIR-radio SEDs for three 850 μm detected galaxies with known AGN. Large plus signs represent *IRAS* and SCUBA data, asterisks show *ISO* data, and the radio observations are shown as small plus signs. The solid line for NGC 4278 corresponds to a spectral index of 0.5. In all cases, the AGN could significantly contribute to the 850 μm fluxes. The large scatter in the radio data for NGC 4261 is attributable to the presentation of a combination of total and nuclear fluxes.

Chapter 4

Dust Models

4.1 Monte Carlo Model

A three-dimensional Monte Carlo radiation transfer code supplied by Kenneth Wood (Bjorkman & Wood, 2001) was used to model the mass and spatial distribution of diffuse dust in a sample of elliptical galaxies. The simulation follows individual photon 'packets' as they are scattered or absorbed by a specified dust distribution at locations governed by the optical depth. When a packet is absorbed, it raises the temperature of an individual grid cell. Radiative equilibrium is enforced by immediately re-radiating the absorbed packet at a new frequency so that the heating and cooling are balanced. The frequency of the re-radiated packet is chosen to correct the cell's previously emitted spectrum to the new temperature. As the simulation proceeds, the entire dust distribution heats up and relaxes to an equilibrium temperature. Eventually, all of the photon packets propagate to the edge of the computational grid, and the calculation ends.

The stellar photons are produced according to a volume emissivity function that was modified to follow an oblate Jaffe law (Capaccioli *et al.*, 1993), which yields a

reasonably good fit to optical surface photometry of typical elliptical galaxies:

$$\rho = \rho_0 \frac{R_J^4}{m^2(m^2 + R_J^2)}, \tag{4.1}$$

with

$$m^2 \equiv x^2 + y^2 + \frac{z^2}{c^2}, \tag{4.2}$$

where x, y and z are the three dimensional coordinates, and c is the intrinsic flattening. For spherical distributions, the Jaffe radius (Jaffe, 1983), R_J, is related to the effective radius, r_e, by

$$R_J = \frac{r_e}{0.763}, \tag{4.3}$$

and the scaling factor ρ_0 is calculated to be:

$$\rho_0 = \frac{L}{2\pi^2 R_J^3 c}, \tag{4.4}$$

where L is the total stellar luminosity, which is divided equally among a specified number of photon packets. The collective spectrum is that of a 10^{10}-year-old starburst (Bruzual A. & Charlot, 1993). The size of each model is limited by an outer cut-off radius, where the emissivity is set to zero. The cut-off radius for the stellar component is arbitrarily set to $5R_J$ in all models, where ρ has fallen to $\sim 10^{-7}$ of the maximum value.

Details of the various dust distributions that were investigated are discussed below. The grain sizes and the scattering and absorption properties of the dust are those of Kim *et al.* (1994). The code is three-dimensional, but azimuthal symmetry has been assumed, with a 200×200×1 grid in spherical coordinates. Radiation transfer is not carried out in the central grid cell and it does not contain stars or dust, because it is a remnant of an earlier version of the code which was used to model scattering in circumstellar disks. The large volume of the modeled galaxies ensures that this simplification does not change any results. Because the various dust distributions explored here are all diffuse and spatially extended, large numbers of photon packets ($\sim 10^8$) are required to ensure that each grid cell reaches an equilibrium temperature. In order to reduce computational runtime, the dust cut-off radius in all models is set to $2R_J$, which generally does not affect the results because of the small contribution from dust at $r \geq 2R_J$. For the Standard Model, described in Section 4.2.2, the density at $2R_J$ has fallen to ($\sim 10^{-6}$) of the maximum value.

In order to increase the efficiency of the original Monte Carlo code, it has been modified to run in parallel and average the results from several processors using different random number seeds to generate photons.

4.1.1 Model Outputs

An emergent SED is constructed as the individual photon packets escape the computational grid at unique frequencies. Because photons leaving the grid have known positions and directions, synthetic images and fluxes can be determined for astro-

nomical filter passbands[1] at a specified viewing geometry. The images produced in all models measure 200×200 pixels, which results in varying angular resolution, depending on the distance to the galaxy and the Jaffe radius. The pixel scales of the synthetic images ranges from 0.22 to 4.7″/pixel, and have an average of 1.6″/pixel. Since the model pixel scales are similar to the seeing in which optical observations are obtained, no attempt was made to convolve the model optical images for comparison. Although seeing is not a concern for the sub-mm and far-IR images investigated below, the resolution of the observational instruments is an important factor. In order to properly compare the synthetic SCUBA and *Spitzer* 70 μm images to the observations, the modeled images were convolved with the appropriate telescope point spread functions (PSF). Convolution was carried out in IDL with the CONVOL routine with a Gaussian function having the measured FWHM of the telescope: 14.5″ for the 850 μm SCUBA images (Sandell & Weintraub, 2001) and ∼18″ for the *Spitzer* 70 μm images (Temi *et al.*, 2007).

One advantage of having a three-dimensional model is that each grid cell can have a unique dust temperature, which is a significant improvement over the one or two temperature models that are commonly used to interpret sub-mm observations of galaxies. To facilitate the comparison of models, an average mass-weighted temperature is calculated for the entire grid. It is presented as T_{std} in Table 4.1.

The synthetic optical images can be used to calculate the colour gradients induced by the model dust distributions. For simplicity, the stellar population is assumed to be

[1]The SCUBA filter profiles used in the model calculations are for the upgraded wideband filters instead of the narrowband filters used for the observations of this study. Since both profiles are reasonably symmetric, the differences are negligible. For a 25 K modified Planck function (Section 4.2.1) the difference in 850 μm flux density is less than 0.3%.

uniform throughout the entire galaxy, so any radial change in colour will be produced solely by dust absorption. Surface brightness profiles for model images are determined using the *ellipse* tool in IRAF and gradients are then extracted in the colour index $B - R$.

4.2 Model Results

Of the 23 galaxies observed with SCUBA, 15 were detected by *IRAS* at 60 and 100 μm. These detections were taken to be the minimum amount of data required to attempt to model the dust distribution in each galaxy using the Monte Carlo code.

4.2.1 Single Temperature Model

For comparison with the Monte Carlo simulations, the average temperature and mass of dust in each galaxy can be estimated by fitting traditional single-temperature dust models to the *IRAS* 60 and 100 μm fluxes. By means of the method of Fich & Hodge (1991), the temperature is calculated by fitting a modified Planck function to the observations, and the mass is given by:

$$M_d = \frac{4a\rho}{3Q_{em}} \left[\frac{S_\nu D^2}{B_\nu(T)} \right], \tag{4.5}$$

with the emission efficiency, Q_{em}, given by,

$$Q_{em} = Q_0 a \left(\frac{250}{\lambda} \right)^\beta. \tag{4.6}$$

Galaxy	T_{IRAS}	T_{Std}	T_{Std}/T_{IRAS}	M_{IRAS}	M_{Std}	M_{Std}/M_{IRAS}
NGC 1339	28.5	25.5	0.89	6.71E+04	7.14E+04	1.10
NGC 1400	25.3	22.9	0.90	7.27E+04	7.16E+04	0.98
NGC 2693	26.2	23.6	0.90	3.53E+06	2.56E+06	0.72
NGC 2974	27.3	26.9	0.99	3.86E+05	1.92E+05	0.50
NGC 3156	25.8	23.8	0.92	3.65E+05	2.81E+05	0.77
NGC 3265	34.5	30.9	0.90	4.06E+05	7.23E+05	1.80
NGC 3377	23.4	23.1	0.99	1.55E+05	3.88E+04	0.25
NGC 3872	23.2	24.6	1.10	2.27E+06	7.78E+05	0.34
NGC 4261	32.9	19.1	0.58	3.58E+04	1.00E+05	2.80
NGC 4278	28.4	24.3	0.86	2.10E+05	2.14E+05	1.02
NGC 4697	29.2	21.5	0.74	9.07E+04	1.69E+05	1.86
NGC 4786	27.0	24.6	0.91	3.65E+06	3.08E+06	0.84
NGC 5353	26.6	31.4	1.20	1.24E+06	2.60E+05	0.21
NGC 6524	30.4	18.1	0.59	2.23E+07	2.40E+08	11
UGC 7354	37.9	17.1	0.45	2.66E+04	6.46E+06	240

Table 4.1: Temperature and mass estimates from single-temperature fits to the *IRAS* data (β=1.5) and from the Standard Model. Setting β=2.0 decreases the temperature and mass estimates by ~7%. All temperatures are in K and all masses are in $M_\odot$.

a is the radius of the grains, ρ is the density (taken to be 3 g cm^{-3}), S_ν is the flux density, D is the distance to the galaxy, and $B_\nu(T)$ is the Planck function. Q_0 is a scaling parameter (set to 40 cm^{-1}), and λ is the wavelength of the emission in microns. The exponent β governs the emissivity of the grains, and is generally taken to be between 1.0 and 2.0. The dust masses and temperatures found in Table 4.1 are for a β value of 1.5. A value of β=2.0 results in a $\sim$ 7% decrease in the temperature and mass estimates.

It should be noted that the derived dust masses are proportional to the distances squared, which can result in large uncertainties in the absolute mass estimates. If they are available, surface brightness fluctuation measurements are the preferred distance indicator in this study, and they generally agree to within 10% or better, but other

distance estimates, such as the Hubble flow method, often only agree with surface brightness fluctuations to within 30-40%. These distance uncertainties can result in mass uncertainties of up to a factor of $\sim$2. With this in mind, mass ratios (which are distance-independent) are used to compare the results of different models. The temperature estimates are not affected by distance.

In principle, the single temperature fits are exact, since there are two fitting parameters for two data points, and they can be used to predict fluxes at longer wavelengths (Table 4.2). The three detected galaxies with known AGN (NGC 4261, 4278, 5353) all have observed 850 μm fluxes that are larger than the predictions of the single temperature model, consistent with the view that the AGN are contributing to the fluxes, as discussed in Section 3.1. The observed fluxes of the remaining detected galaxies are all consistent with the predictions for β=1.5, but are larger than the predictions for β=2.0. For the 9 non-detected galaxies, the SCUBA upper limits are consistent with the predictions for β=1.5 in 4 of the cases, and in all but one case for β=2.0. The only exception is NGC 1400, which is a possible detection at 23 mJy (2.4σ). The SCUBA image is not convincing, but if it is a detection it would bring the observed value closer to agreement with the predictions.

In summary, a β value of 2.0 predicts fluxes that are in better agreement with the 850 μm upper limits, but in the case of detections, setting β=1.5 provides better agreement. It could possibly show that β varies from galaxy to galaxy, reflecting differences in dust properties, and the SCUBA detections have preferentially selected galaxies with low β values. It could also be interpreted that elliptical galaxies are better fit with higher values of β, and the fact that the detections disagree with the

Galaxy	F_{850} (mJy) observed	F_{850} (mJy) β=2.0,1.5	F_{450} (mJy) observed	F_{450} (mJy) β=2.0,1.5
NGC 2974	19 ± 5.6	10 - 21	< 200	87 - 140
NGC 3265	34 ± 7.8	12 - 28	< 160	120 - 200
NGC 4261	180 ± 17	0.52 - 1.1		5 - 8
NGC 4278	48 ± 8.5	11 - 25	< 73	100 - 170
NGC 5353	48 ± 9.6	9.6 - 21	< 320	86 - 140
NGC 6524	70 ± 3.9	40 - 88	356 ± 73	380 - 610
NGC 1339	< 8.7	3.8 - 8.4	< 160	35 - 57
NGC 1400	< 9.5	30 - 66	< 40	270 - 430
NGC 2693	< 16	7.2 - 16	< 120	64 - 100
NGC 3156	< 11	7.8 - 17	< 70	69 - 110
NGC 3377	< 7.9	11 - 25	< 100	97 - 160
NGC 3872	< 9.8	10 - 22	< 180	88 - 140
NGC 4697	< 18	8.3 - 18		77 - 120
NGC 4786	< 12	9.4 - 20		84 - 140
UGC 7354	< 10	2.2 - 4.8	< 73	22 - 34

Table 4.2: SCUBA observations compared to predicted 450 and 850 μm flux densities for single-temperature fits to *IRAS* data. The first values in columns 3 and 5 correspond to setting β=2.0 and the second values are for β=1.5. Note that NGC 1400 is a possible detection at 850 μm (23 mJy or 2.4σ) and that the 850 μm flux of NGC 6524 could be underestimated by 30-40%.

predictions for a high β value could be evidence that the 850 μm fluxes are enhanced by additional sources of emission.

4.2.2 Standard Model

In normal elliptical galaxies that have not undergone a recent merger, the majority of interstellar dust is thought to originate from mass loss in the evolving population of red giant stars. This idea is supported by observations of elliptical galaxies from the *ISO* satellite between 9 and 15 μm that reveal excess emission relative to photospheric levels and emission features believed to be associated with silicates in circumstellar envelopes (Athey *et al.*, 2002). Further support for a circumstellar origin for the emission comes from the mid-infrared surface brightness profiles, which follow a similar de Vaucouleurs $R^{1/4}$ law as the stellar component (Athey *et al.*, 2002). As a result, it was decided that the starting point in the exploration of dust distributions would be to give the stellar content and dust the same Jaffe radius (i.e. the stars and dust are co-spatial). It will be referred to as the *Standard Model.* The stellar distribution is cut-off at $5R_J$ and the dust distribution is cut off at $2R_J$ to decrease computational runtime. The true shapes and inclinations of the galaxies are unknown; in all models the viewing direction is assumed to be edge-on (i.e. in the x, y plane of Equation 4.2), with the axial ratio given in Table 2.1. The parameter c in Equation 4.2 represents the axial ratio, or degree of flattening in the z direction.

The SEDs of the 15 galaxies chosen for modelling are presented in Appendix B. The optical and 2MASS (Two Micron All Sky Survey) data are taken from the NED.

The *IRAS* fluxes, listed in Table 3.1, are from Bregman *et al.* (1998) if available, or from the NED, otherwise. *ISO* observations of NGC 4261, 4278, 4697, 5353 are from Temi *et al.* (2004), *Spitzer* observations of NGC 2974 and NGC 3265 are from Kaneda *et al.* (2007) and Dale *et al.* (2005), respectively.

For the observed fluxes and the galaxy properties in Table 2.1, the only variable that remains in the Standard Model is the dust mass. An attempt was made to adjust the mass to fit the *IRAS* 60 and 100 μm observations equally well, as judged by eye. In general, the SEDs predicted by the Standard Model are inconsistent with the observations and have a negative slope between 60 and 100 μm, while the *IRAS* measurements have a positive slope. In almost all cases, the model predicts a peak in dust emission around 60 μm while the observed SEDs generally peak around 100 μm, which implies that the models contain too much warm dust[2]. Such experiments with the Standard Model show that, with the possible exception of NGC 3265 and NGC 4697, it is not possible to reproduce the observed SEDs of elliptical galaxies with a dust distribution that is co-spatial with the stellar content.

There is clearly a wide variety in the SEDs of the 15 galaxies presented in Appendix B. Based on the classifications given in Table 2.1, three galaxies are likely S0s (NGC 3156, NGC 5353, NGC 6524). The SEDs of two additional galaxies, NGC 4261 and UGC 7354, are unusual, and deviate significantly from the predictions of the Standard Model dust distribution. Excluding those 5 galaxies, the Standard Model predicts average dust temperatures that are generally $\leq 10\%$ lower than those implied by the *IRAS* observations alone, whereas the model dust masses agree with the single-

[2]The models of NGC 6524 and UGC 7354 are exceptions; they do not contain enough warm dust.

temperature predictions to within a factor of ~2. The mass and average temperature predicted by the Standard Model for each galaxy can be found in Table 4.1. While the Standard Model provides a logical starting point in the exploration of diffuse dust distributions in elliptical galaxies, the calculated SEDs do not generally fit the observations.

4.2.3 Alternative Dust Distributions

To improve upon the Standard Model fits, two alternative dust distributions were explored for five of the sample galaxies that had additional information available from optical colour profiles (NGC 2693, 3377, 4278) and/or other FIR observations (NGC 2974, 4697). All alternative simulations are identical to the Standard Model, except for the assumed dust volume density distribution. It should be noted again that the absolute dust mass estimates are dependent on distance uncertainties, but mass ratios, temperatures, and fluxes can be compared reliably between models. In an effort to remove the warmest dust from the distribution and thereby shift the predicted dust emission peak to longer wavelengths, a set of models were calculated with a central dust cavity. In these models, the Jaffe radii of the stars and dust remained equal, but the dust density inside a central cut-off radius was set to zero; they are referred to as *Central Cavity Models.*

By varying the central cut-off radius and total mass, the average dust temperature can be lowered and the thermal emission peak shifted to longer wavelengths, which provides much better agreement with the observed SEDs (dot-dashed curves in Figure

Galaxy	R_J	$R_{cut-off}$	$R_{cut-off}/R_J$
NGC 2693	9.42	2.50	0.27
NGC 4278	3.20	1.00	0.31
NGC 4697	5.35	1.25	0.23
NGC 2974	3.33	1.50	0.45
NGC 3377	2.48	0.50	0.20

Table 4.3: Inner cut-off radius (in kpc) for the dust distribution in the Central Cavity Models.

Galaxy	T_{IRAS}	T_{Std}	T_{Inv}	T_{CC}	T_{Inv}/T_{IRAS}	T_{CC}/T_{IRAS}
NGC 2693	26.2	23.6	18.7	21.1	0.71	0.81
NGC 4278	28.4	24.3	19.8	22.0	0.70	0.77
NGC 4697	29.2	29.2	17.9	20.6	0.61	0.71
NGC 2974	27.3	21.5	21.3	23.1	0.78	0.85
NGC 3377	23.4	23.1	19.0	22.2	0.81	0.95

Table 4.4: Comparison between single-temperature fits to the *IRAS* data and mass weighted temperatures (in K) from the Standard Model, the Inverse Model, and the Central Cavity Model.

Galaxy	M_{IRAS}	M_{Std}	M_{Inv}	M_{CC}	$\frac{M_{Inv}}{M_{IRAS}}$	$\frac{M_{CC}}{M_{IRAS}}$
NGC 2693	3.53E+06	2.56E+06	2.22E+07	1.24E+07	6.3	3.5
NGC 4278	2.10E+05	2.14E+05	2.02E+06	1.12E+06	9.6	5.3
NGC 4697	9.07E+04	1.69E+05	1.11E+06	5.75E+05	12	6.3
NGC 2974	3.86E+05	1.92E+05	1.62E+06	1.10E+06	4.2	2.8
NGC 3377	1.55E+05	3.88E+04	3.43E+05	1.81E+05	2.2	1.2

Table 4.5: Comparison between the dust mass (in $M_\odot$) derived from single-temperature fits to the *IRAS* data and the mass from the Standard Model, the Inverse Model, and the Central Cavity Model.

4.1). The best-fitting central cut-off radius, chosen by eye-fits to the data, is listed in Table 4.3. It is generally about one quarter of the Jaffe radius. The Central Cavity Model predicts average mass-weighted temperatures that are about 10-20% lower than the single-temperature model fit to the *IRAS* data alone, and masses that are about 4 times greater (see Table 4.4 and Table 4.5). The properties of the images produced by all models are discussed below.

Temi *et al.* (2007) provide a possible explanation for a central dust cavity. They suggest that dust ejected from stars within the central ~kpc of a galaxy could be dense enough to undergo cooling, and fall to the centre, where concentrated nuclear disks are often observed. They propose that the material contained in the central disk could then be buoyantly transported to large radii (several kpc) by intermittent AGN activity. The concept of a central dust cavity in elliptical galaxies is supported by the excellent agreement of the model SEDs presented in this section with the observations.

A second scenario that improves the quality of the predicted SEDs is a dust volume density distribution that decreases with radius as $\rho \propto r^{-1}$, which is referred to as the *Inverse Model.* Such a dust distribution is known to produce linear colour gradients in log(r) (Wise & Silva, 1996), which are consistent with observations of elliptical galaxies. Compared to the Standard Model, the Inverse Model also shifts dust away from the centre of the galaxy, where it is warmest, and produces SEDs that are in much better agreement with the observations (dotted curves in Figure 4.1). On average, the mass-weighted temperature predicted by the Inverse Model is about 20-30% lower than the single temperature fit to the *IRAS* data, and the mass

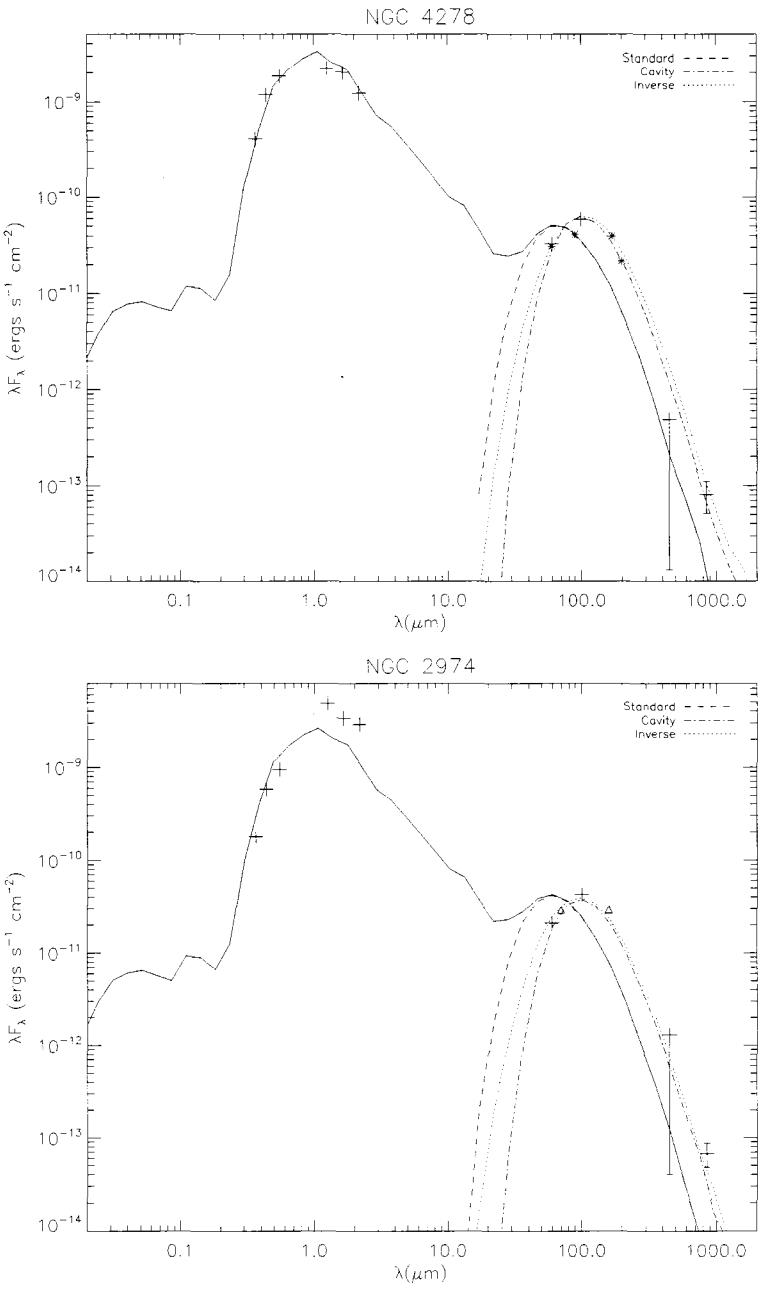

Figure 4.1: a.) Model SED comparison for the three dust distributions. The asterisks represent *Spitzer* data and the triangles represent *ISO* data. The solid curves represent the total output flux from the Standard Model. The error bars for the 850 μm observations and all upper limits correspond to the standard deviations listed in Table 3.1; error bars not shown are smaller than or comparable to the symbol size. Compared to the Standard Model, the two alternative models contain relatively cool dust, which shifts the thermal emission peak to longer wavelengths, in better agreement with the observations. It is not understood why the 2MASS observations of NGC 2974 do not agree with the input stellar SED.

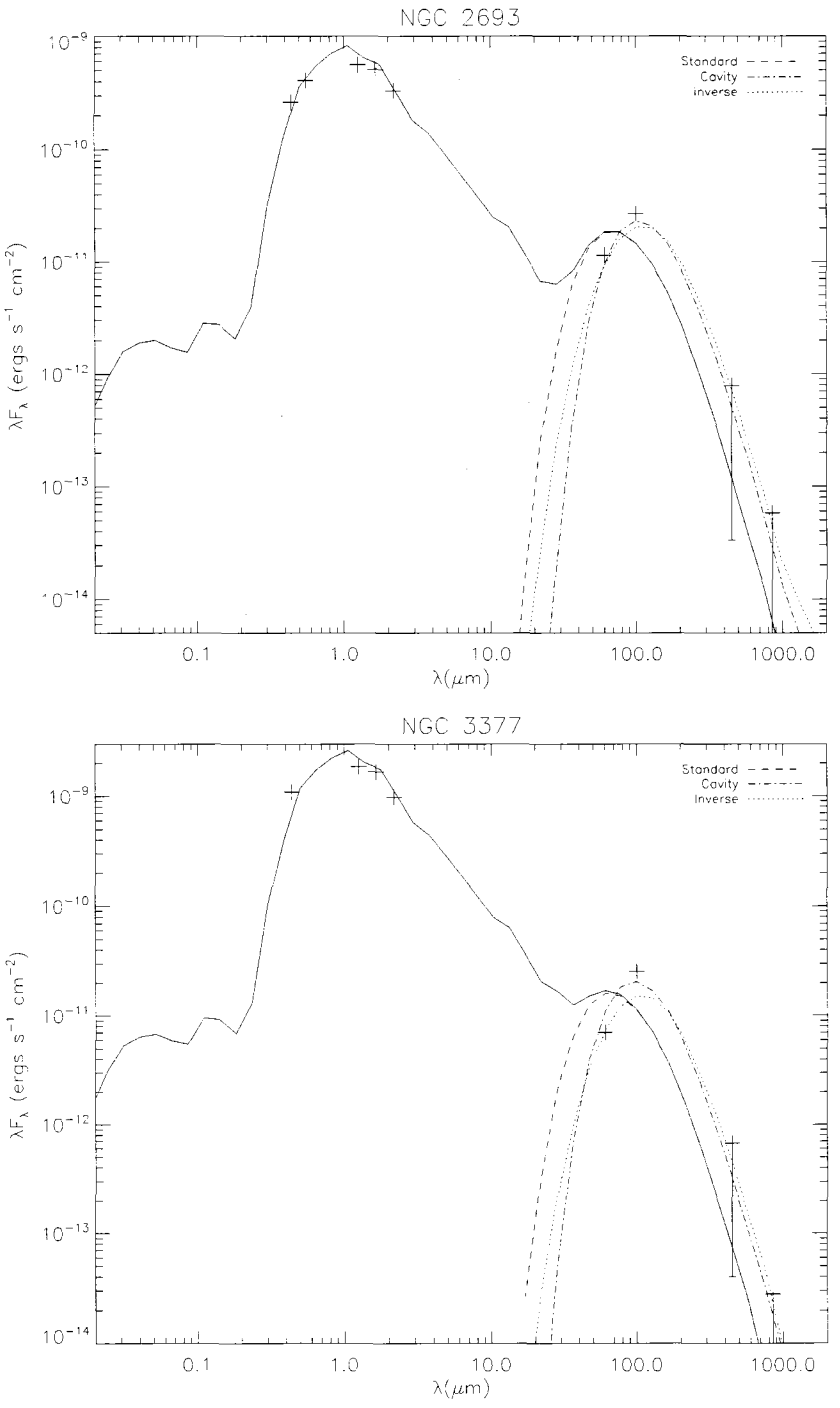

Figure 4.1: b.) (*cont'd*) Model SED comparison.

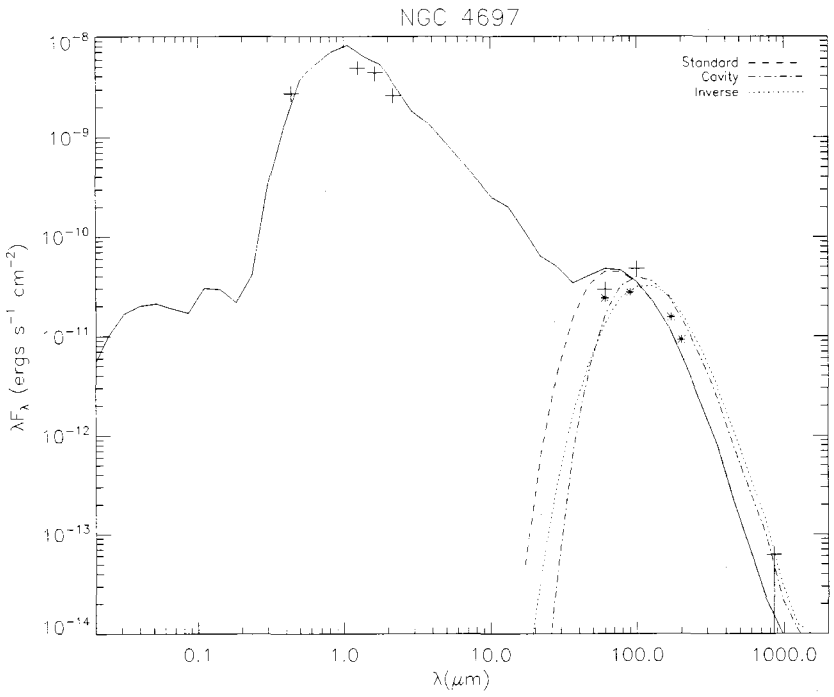

Figure 4.1: c.) (*cont'd*) Model SED comparison.

is about 7 times greater (see Table 4.3 and Table 4.4). The dust mass determination has a fairly large uncertainty associated with it. In the Standard and Central Cavity Models the choice of an outer cutoff radius (set to $2R_J$) did not affect the dust mass determination because of the rapid decline in volume density with radius. Because of the gradual radial decline of the dust density in the Inverse Model, the choice of an outer cutoff radius introduces an uncertainty in mass of a factor of $\sim$2.

The lower temperatures and higher masses predicted by the two alternative dust distributions are consistent with the results of a two-component model fit to *ISO* data by Temi *et al.* (2004). They report dust masses that are often an order of magnitude larger than what is estimated from the *IRAS* fluxes alone, and those conclusions are supported by the results of the Monte Carlo simulations for the five elliptical galaxies

presented here.

In summary, the average dust masses predicted by the Standard Model are consistent with single temperature fits to the *IRAS* data to within a factor of ~2, and the Central Cavity and Inverse Models predicts masses that are about 4 and 7 times greater.

4.2.4 Synthetic Dust Images

The synthetic images produced in the modelling process provide additional information on the dust distributions that can be compared to observations. It was hoped that SCUBA could provide images of the dust, but the fluxes are too low to constrain the surface brightness profiles needed for comparison. The detections are either near the sensitivity limit of the exposures, or the interpretation of the source of emission is clouded by the possibility of contamination from an AGN point source.

In the absence of suitable SCUBA images, the *Spitzer* 70 μm images obtained by Temi *et al.* (2007), with a PSF FWHM of 18″, provide the best available constraint on the spatial extent of dust emission in elliptical galaxies. They observed a sample of 46 elliptical galaxies at 70 μm and detected extended emission in many of them with an instrument convolved FWHM of 20-23″ and a FW0.1M of 40-60″. There are only two galaxies in common between their sample and the SCUBA sample investigated here: NGC 2974 is observed to have a FWHM of 22.8″at 70 μm, and NGC 4697 is observed to be a point source. Figure 4.2 shows the surface brightness profiles of the convolved 70 μm synthetic images for the three dust distributions that are considered,

along with the PSF that is used for the convolution.

In all 5 galaxies selected for detailed study (Table 4.2), the relatively centrally concentrated dust distribution of the Standard Model predicts convolved synthetic 70 μm images that are consistent with point-like sources. Of the two alternative dust distributions, the Inverse Model predicts 70 μm surface brightness profiles that are in better agreement with the FWHM and FW0.1M measurements of Temi *et al.* (2007). Even though there is little overlap between the two samples, the Central Cavity Model produces profiles that are often more extended than what has been observed in elliptical galaxies with *Spitzer*. For the two galaxies where direct comparisons can be made, the Inverse Model is more consistent with the observations. For NGC 2974 the measured FWHM of 22.8″ is reproduced by the Inverse Model, while the Central Cavity Model predicts a much larger value. NGC 4697 is observed to be a point source at 70 μm, and though both models predict a FWHM that is significantly larger than the PSF, the Central Cavity Model is much more extended.

4.2.5 Colour Gradients

The colour gradients induced by the various diffuse dust distributions for the three galaxies with comparable observations (NGC 4278, 3377, 4697) are presented in Figure 4.3. The observed gradients are taken from Peletier *et al.* (1990). A shift of +0.17 magnitudes has been applied to all of the synthetic colours to scale them to the Peletier *et al.* (1990) sample. While the colour gradients induced by the distributions considered here extend over similar radial scales as those observed, they only

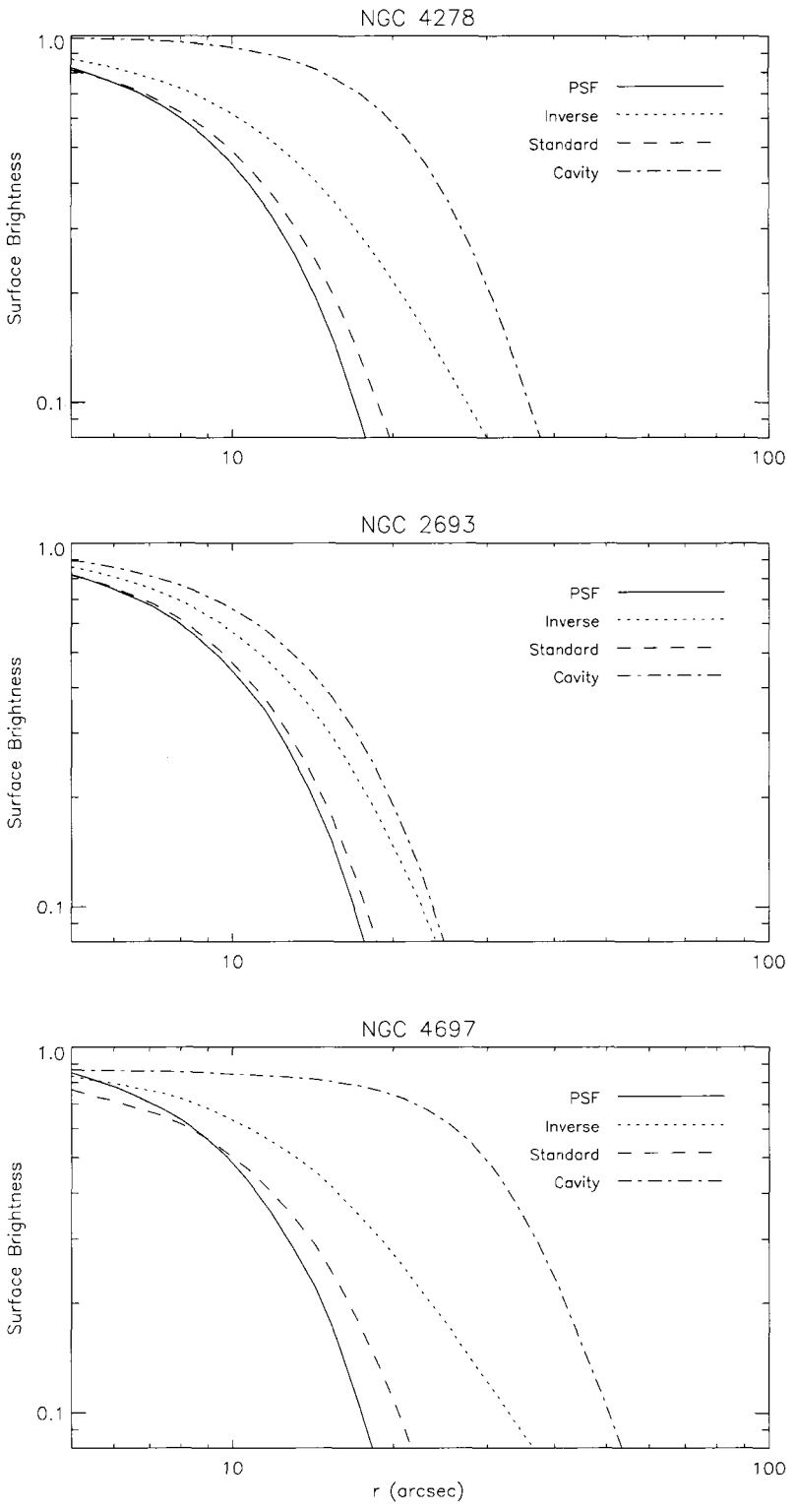

Figure 4.2: a.) Predicted *Spitzer* 70 μm surface brightness profiles for the various dust distributions. All profiles are normalized to unity at the center.

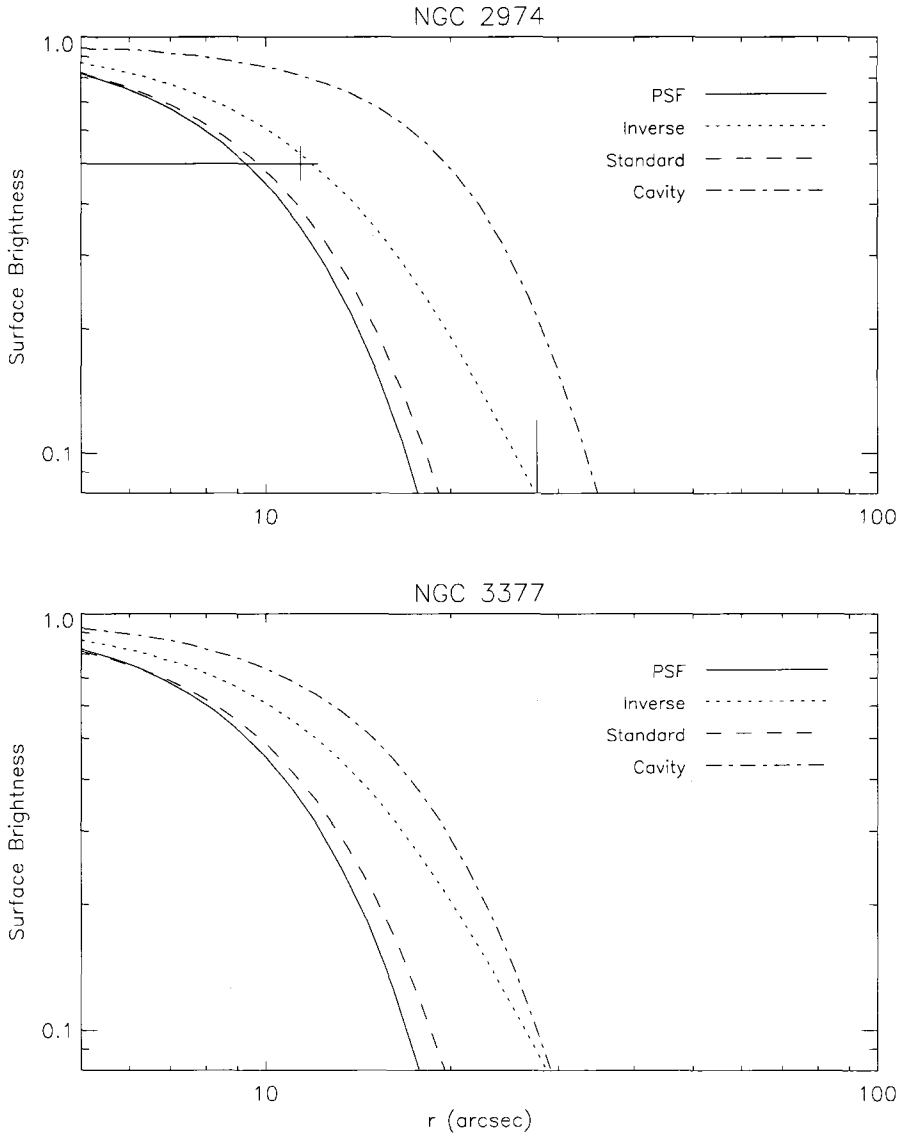

Figure 4.2: b.) (*cont'd*) Predicted *Spitzer* 70 μm surface brightness profiles. The solid vertical line for NGC 2974 corresponds to the measured FW0.1M of 55.4″ and the cross connected to the solid horizontal line represents the measured FWHM of 22.8″ (Temi *et al.*, 2007).

account for a small fraction of the total gradients. The Standard Model for NGC 4697 is the only exception, where the large angular extent of the galaxy ($R_J = 93.4''$) has allowed a steep gradient, confined to the central regions ($r \leq 25''$) by the concentrated dust distribution, to be resolved.

From the Monte Carlo simulations presented here, it appears that a diffuse dust distribution, capable of reproducing the observed SEDs of normal elliptical galaxies, will not significantly affect the measured colour gradients. This result is in contrast to the suggestion of Wise & Silva (1996), who propose that dust distributions with a $\rho \propto r^{-1}$ decline are capable of reproducing observed colour gradients with total dust masses that are on the order of those inferred by *IRAS* observations. For the same set of observations (the Peletier *et al.* (1990) sample), the Monte Carlo simulations indicate that the total dust mass required to reproduce the colour gradients is ~1-2 orders of magnitude larger than the *IRAS* estimates. The discrepancy in dust mass with Wise & Silva (1996) can be traced to inconsistencies in their choice of an outer cut-off radius for the $\rho \propto r^{-1}$ distribution. The models they use to infer the required optical depth are calculated with an outer cut-off radius of 100 kpc, but when converting to a total dust mass, they only integrate the density out to the maximum radius for which the colour gradient has been measured (~10 kpc), and neglect the outer ~90%. It is stated that the derived dust masses correspond to the minimum values required to reproduce the observed colour gradients, but it should be pointed out that these masses actually have a small effect on the measured gradients, and the density distribution needs to be integrated to the same outer radius that was used to determine the optical depth.

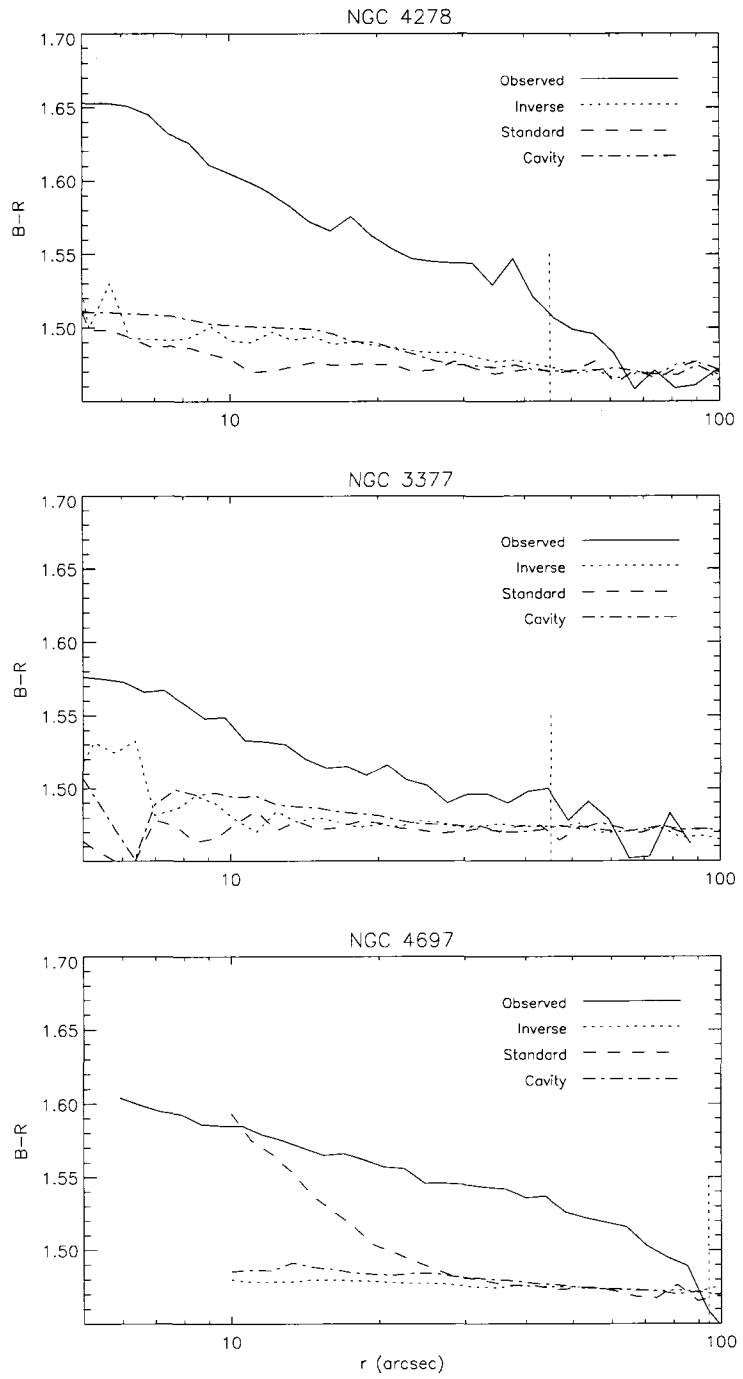

Figure 4.3: Synthetic B-R colour gradients induced by the three dust distributions compared to the observations of Peletier *et al.* (1990). The vertical dashed line in each panel corresponds to the measured Jaffe radius. The large changes in B-R at small radii, especially noticeable for NGC 3377, are thought to be due to an insufficient number of photon packets in the simulations.

In the absence of a substantial impact from diffuse dust, the observed colour gradients can almost entirely be attributed to radial changes in stellar populations, which has been done in the past, when the effects of dust were largely unknown. While it is still possible that diffuse dust could affect early-type galaxies containing significantly more dust than those considered here, unusually dusty galaxies are expected represent a small minority of systems.

4.2.6 Stellar Mass Loss

If the diffuse dust in elliptical galaxies is associated with gas that has been returned to the ISM as a product of stellar evolution, it is possible to estimate how much dust should have been deposited throughout the evolution of the galaxy. For a simple, closed box, view of elliptical galaxy evolution, the mass of returned gas (M_r) should scale as $M_r = KL_B$, where L_B is the present blue luminosity. For a 10 Gyr old population of solar mass stars, Faber & Gallagher (1976) found $K \sim 0.1$. Ciotti *et al.* (1991) revised the monolithic model with updated return rates and included the contributions of a range of stellar masses given by a Salpeter initial mass function (after 1 Gyr only the $\sim$0.85-1.75$M_\odot$ stars contribute). If the ISM is initially removed in a hot, outflowing wind produced by Type II supernovae heating, but all material returned after 0.5 Gyr is retained, the approximation of Ciotti *et al.* (1991) gives $K = 1.2$ (Welch & Sage, 2003), for a 10 Gyr old population.

Figure 4.4 shows the mass of dust derived from FIR observations as a function of blue luminosity. The solid line represents the predicted dust mass associated with

stellar evolution for $K = 1.2$ and a typical gas to dust mass ratio of 100[3]. The dashed line represents 1% of the predicted dust mass; most of the dust returned to the ISM of elliptical galaxies from stellar mass loss has been removed, rendered unobservable at FIR/sub-mm wavelengths, or destroyed. Dust destruction is likely the dominant factor, with two known causes: (1) dust grains are destroyed through collisions with ions (sputtering) in the hot X-ray emitting gas present in elliptical galaxies (Draine & Salpeter, 1979), and (2) intense radiation from an AGN can also destroy dust grains (Freudling *et al.*, 2003). It is interesting to note that the two galaxies containing the least amount of gas compared to the predictions are both known X-ray sources with diffuse components (NGC 4261 and NGC 4697; shown as squares in Figure 4.4). Also contributing to the severe deficiency of dust in NGC 4261 is a luminous AGN that dominates the 850 μm flux (see Section 3.1).

Figure 4.4 closely resembles analogous figures in Welch & Sage (2003), and Sage *et al.* (2007) showing cool gas in E/S0 galaxies. A similar upper cutoff appears to be present in the ISM content of elliptical galaxies as measured by both gas and dust. For the 5 galaxies studied in greater detail in Section 4.2.3, the large dust masses predicted by the alternative distributions are generally consistent with the H I masses that have been observed in these systems (for an assumed gas to dust mass ratio of 100, and scaled to the distances used in this study): $1.4\times10^{9}M_{\odot}$, $6.53\times10^{8}M_{\odot}$, $<1.1\times10^{7}M_{\odot}$, $5.5\times10^{8}M_{\odot}$, $<3.8\times10^{8}M_{\odot}$ for NGC 2693, 2974, 3377, 4278, 4697 (Huchtmeier *et al.*, 1995; Knapp *et al.*, 1979; Gallagher *et al.*, 1975). Comparable amounts of gas and dust are expected if both components have similar origins and are well-mixed.

[3]This value is appropriate to the Milky Way and is highly uncertain.

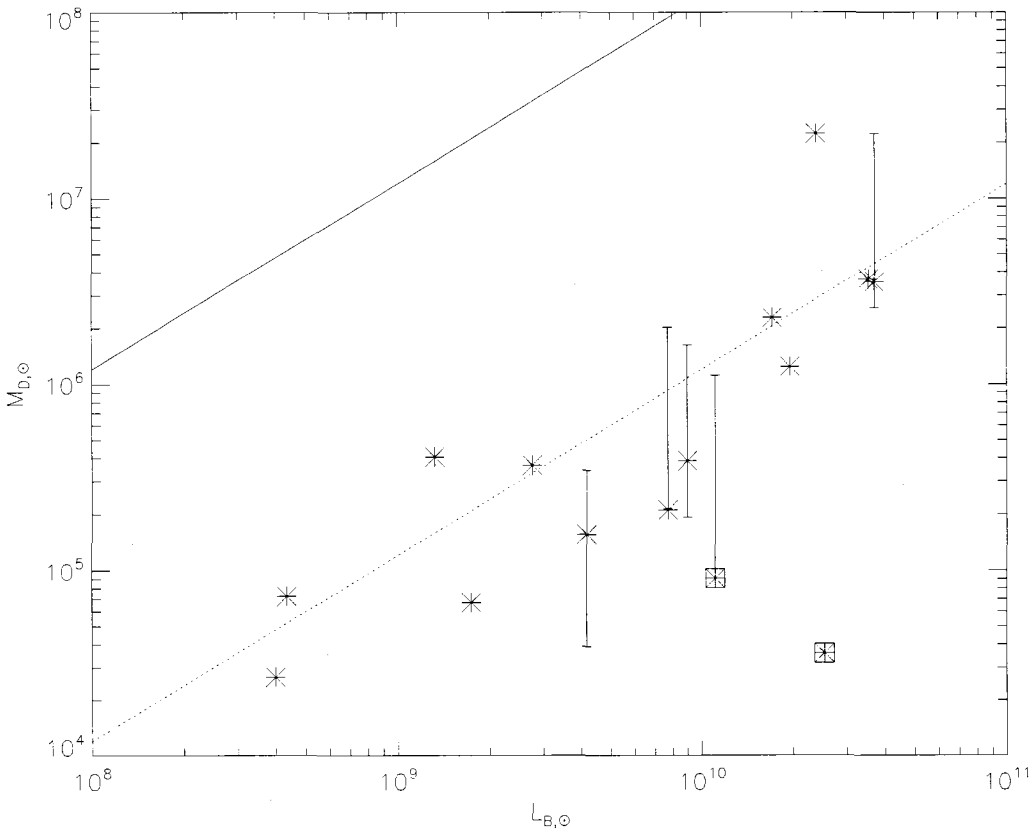

Figure 4.4: Dust masses derived from FIR/sub-mm emission compared to the predictions from stellar mass loss. The single temperature dust mass estimates from Section 4.2.1 are shown as asterisks. The vertical error bars represent the range of dust mass estimates from the Monte Carlo models for the five galaxies studied in greater detail. The solid line is the Ciotti *et al.* (1991) prediction for the dust mass returned to the ISM between 0.5 and 10 Gyr (with a gas to dust ratio of 100), and the dashed line shows 1% of the predicted amount. The two boxed points represent NGC 4697 and NGC 4261, which are both diffuse X-ray sources; NGC 4261, the lower point, at $L_{B,\odot} \sim 2.5 \times 10^{10}$, also hosts a bright AGN.

Chapter 5

Discussion and Conclusions

A sample of 23 early-type galaxies was searched for extended emission from diffuse dust at 450 and 850 μm with the SCUBA instrument on the *JCMT*, which resulted in 5 detections at 850 μm and 1 detection at both 850 and 450 μm. The SCUBA images of the detected galaxies contain little convincing structure, and most either contain known AGN, which possibly contaminate the 850 μm flux densities, or are relatively gas-rich S0s. Low surface brightness flux from extended diffuse dust in early-type galaxies is undetected with modest SCUBA integration times.

Three dimensional Monte Carlo models of the FIR/sub-mm SEDs of elliptical galaxies have been calculated, and require dust masses that are often an order of magnitude larger than those inferred from single temperature fits to *IRAS* fluxes alone. The larger masses and cooler average temperatures inferred by the models are consistent with the fact that *IRAS* was not sensitive to dust at temperatures less than $\sim$20 K. For an assumed gas to dust ratio mass ratio of 100, the implied dust masses are also generally consistent with the small sample of H I detections and numerous upper limits that have been observed.

In an effort to fit the observed SEDs, various dust distributions were explored. It was found that dust distributions that are co-spatial with the stellar content contain too much warm dust to match *IRAS* photometry. Alternative distributions that

reduce the amount of warm dust include creating a central cavity in the dust distribution, or requiring that the density declines as $\rho \propto r^{-1}$. Both of these distributions move dust away from the central regions, where the stellar radiation field is most intense, and predict cooler dust temperatures that are capable of reproducing the SEDs. Only a $\rho \propto r^{-1}$ dust distribution was found to predict 70 μm surface brightness profiles that are consistent with the recent *Spitzer* observations of Temi *et al.* (2007); distributions with a central cavity produce highly extended surface brightness profiles that are inconsistent with the admittedly meagre present observations.

Perhaps most importantly, in the Monte Carlo simulations presented here, it was found that the impact of diffuse dust distributions on the radial broadband colour gradients of elliptical galaxies is negligible. This is in contrast to the suggestion of Wise & Silva (1996), who propose that dust distributions with a $\rho \propto r^{-1}$ decline are capable of reproducing observed colour gradients with total dust masses that are on the order of those inferred by *IRAS* observations. The Monte Carlo simulations indicate that the total dust masses required to reproduce the observed colour gradients are $\sim$1-2 orders of magnitude larger than the *IRAS* estimates. The discrepancy in dust mass with Wise & Silva (1996) has been traced to inconsistencies in their choice of an outer cut-off radius for the $\rho \propto r^{-1}$ distribution. Establishing the minor impact of a diffuse dust component on the radial colour gradients of early-type galaxies is important in our understanding of how these galaxies form, and confirms that the gradients are primarily caused by changes in stellar populations.

The origin of a diffuse dust component remains unclear. A considerable amount of dust is expected to be produced in the atmospheres of the evolving stellar popu-

lation, but if the dust is exposed to the hot plasma present in many elliptical galaxies, it should be destroyed by sputtering. Calculations for various dust destruction timescales show that the amount of dust implied by *IRAS* observations is generally greater than what can be accounted for by stellar mass loss (Goudfrooij & de Jong, 1995). This is viewed as evidence that the dust must be acquired from an outside source. The even larger dust masses found in this study enhance the discrepancy, and seem to imply that an external source of dust is necessary. However, if mergers are currently the main source of dust in elliptical galaxies, a continuous supply of dusty satellite galaxies is required to replenish the dust as it is destroyed (Temi *et al.*, 2007); these satellite galaxies are conspicuously absent.

The success of dust distributions that are much more diffuse than the stellar population (e.g. the Inverse Model) in reproducing the observed SEDs also seems to support a merger scenario, since it would be difficult to redistribute internally produced dust to larger galactic radii, but an intriguing suggestion by Temi *et al.* (2007) provides such a mechanism. They suggest that dust ejected from stars within the central ~kpc of a galaxy could be dense enough to undergo rapid cooling (Mathews & Brighenti, 2003), and fall to the centre, where concentrated nuclear disks are often observed. They propose that the material contained in the central disk could then be buoyantly transported to large radii (several kpc) by intermittent AGN activity, which could supply the outer regions of the galaxy with the excess dust required to reproduce the observed FIR fluxes. It is possible that this mechanism could also produce a central cavity, which has been shown here to be capable of fitting the SEDs of several galaxies.

The challenge of understanding galactic formation mechanisms is certainly a growing and exciting field. Elliptical galaxies provide a valuable history of this process, and establishing their origins is essential to our understanding of how galaxies evolve. Studying the ISM of early-type galaxies can provide important information on their origins, but the paucity of gas and dust in these systems will continue to challenge observational capabilities. Newly-commissioned and future detectors, such as SCUBA-2, *AKARI* and *ALMA* will ensure the advancement of observationally driven discovery in this field.

Appendix A

Data Reduction

The reduction of the raw SCUBA data was carried out with SURF and visualization was performed with the Kernel Application Package (KAPPA).

When observations are obtained at 450 and 850 μm, the two observations are stored in one data file. As a result, the first two steps in the reduction process are performed simultaneously on both data sets. The first step is to use the SURF command REDUCE_SWITCH to subtract the off-position observations from the source position. The output is then corrected with the FLATFIELD task using the flat-fields stored in the data files. The next step is to correct for atmospheric extinction.

There are two available methods for determining the opacity of the atmosphere. One method is to perform a skydip with SCUBA, which measures the brightness temperature of the sky over a range of elevations (between $\sim$80 and 15 degrees) near the time of observations. The zenith sky opacity can then be estimated from a model describing both the atmosphere and the optical system. The advantage of this method is that it provides opacity measurements at the observing frequency, but it is also time-consuming to obtain measurements frequently enough to account for time variations in the sky opacity. The alternative is to use the nearby CSO (Caltech Submillimeter Observatory) Tau monitor, which measures the sky opacity every ten minutes at a frequency of 225 GHz. Comparison of the CSO values to the skydip

values at 850 and 450 μm has led to the following scaling relations for the pre-upgrade (October 1999) narrowband filters used in this study:

$$\tau_{850} = 3.99(\tau_{CSO} - 0.004), \tag{A.1}$$

$$\tau_{450} = 23.5(\tau_{CSO} - 0.012), \tag{A.2}$$

To reduce the effects of scatter in the CSO values, polynomials have been fit to the opacity measurements for each night by the *JCMT* staff. The value of the polynomial fit at the start of each observation is provided when downloading the data from the Canadian Astronomy Data Centre (CADC). The values were scaled using the above relations to obtain zenith sky opacities at 850 and 450 μm at the time of observation. A sample of available skydips were reduced independently, and found to be in good agreement with the CSO values. On a few nights when the CSO data were not available, skydips were exclusively used to determine the opacity. With the zenith sky opacity determined, the EXTINCTION task can be used to correct for atmospheric attenuation based on the airmass at the time of the observation. At that point, the 850 and 450 μm data sets are separated because of the differences in opacity between the two wavelengths.

The next step is to identify and remove noisy bolometers from the data set. Ideally, noise measurements are interspersed with observations of the targets for that

purpose. They can be analyzed with the command SCUNOISE to identify bolometers that have high noise levels. Often however, only one noise measurement per night is available. To improve the situation, the extinction-corrected jiggle maps of all the targets from each night were next visually inspected with KAPPA's DISPLAY (fill=true) command, which shows the output of each bolometer as a function of time throughout the observation. That provides a check on the noise measurements, and a method of detecting noisy bolometers that would have been missed if only the noise measurements were employed. Noisy bolometers were removed from the data set with the CHANGE_QUALITY command. In most cases, the removal of bolometers did not produce gaps in the data because the jiggling of the array and the rotation of the sky throughout the observation fills in the 'holes'.

Occasional large spikes in the output from each bolometer are now removed using SCUCLIP, in which the mean and standard deviation of the output from each bolometer are calculated and any values greater than 5σ from the mean are removed. That would be problematic for bright compact sources, since a bolometer could move on and off the source during the jiggle pattern, but the method works well for the faint sources considered here.

The next task is to remove the contribution from the sky with the command REMSKY (add=false), which requires the identification of bolometers that were off-source during the observation. The median value of the sky bolometers for each of the 64 jiggle positions is calculated and then subtracted from the jiggle. Since the sources observed here are expected to be faint and confined near the centres on the galaxies, the 'sky' bolometers are taken to be the outer two (of four) hexagonal rings

of bolometers at 850 μm, and the outer three (of five) rings at 450 μm. Because of the faintness of the sources and the potentially significant contribution from the sky, further care was taken in selecting sky bolometers by again visually inspecting the bolometer outputs using the DISPLAY command. Any sky bolometers that were unusually noisy were not included in the sky calculation. To estimate the importance of the subjective nature of the sky bolometer selection, an additional set of sky bolometers were identified that were 'marginally' noisy. Reductions from that point proceeded along parallel paths: one with the 'marginal' bolometers included in the sky calculation, and another where they were excluded. The process resulted in an average uncertainty in flux density of 0.6 mJy at 850 μm.

Once the contribution of the sky has been removed, each night of observations is then despiked by position on the sky (DESPIKE), where every measurement from each bolometer is placed into a grid, by position on the sky, and compared to all other values from that night that lie in the same region. If a measurement lies more than 3σ from the mean of all the values in a cell, it is considered a spike, and removed. All of the data from one night are then REBINed onto a rectangular grid to create a final map of the observations with 1-arcsecond pixels.

In some cases, observations for individual targets were obtained on multiple nights. In such instances, data from each night was reduced in the manner described above and then averaged using KAPPA, with weighting proportional to the integration times. The command MATHS was used to multiply the images by the weights, and ADD was used produce the final averaged image.

Appendix B

Spectral Energy Distributions

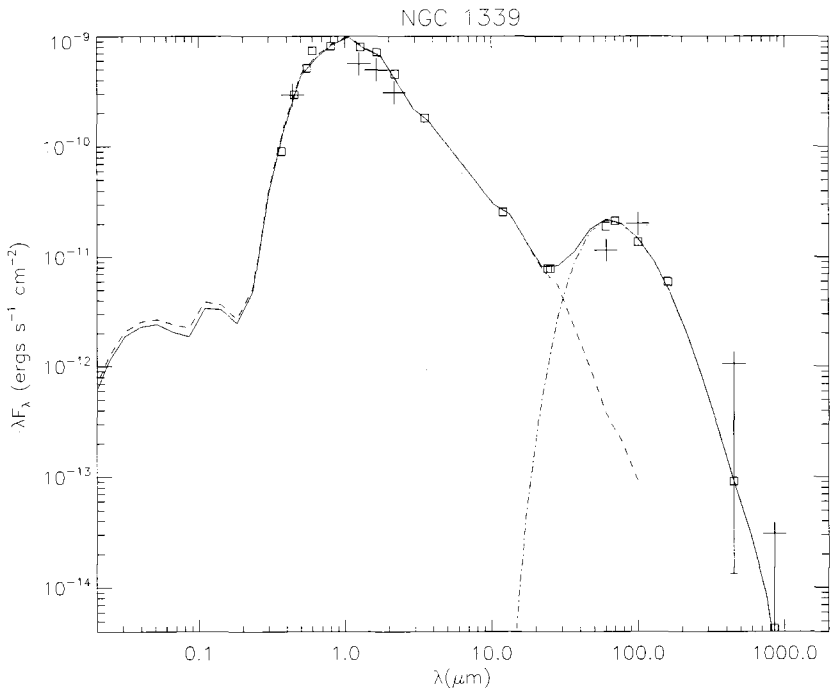

Figure B.1: a.) SEDs for the Standard Model dust distribution. The dashed lines represent the input stellar spectrum, the dash-dot lines represent thermally reprocessed flux, and the solid lines represent the total output spectrum. The open squares show synthetic filter fluxes through various passbands. Spitzer observations are shown as triangles and *ISO* observations as asterisks. Optical, *IRAS* and SCUBA fluxes are indicated by plus signs. The error bars for the 850 μm observations and all upper limits correspond to the standard deviations listed in Table 3.1; error bars not shown are smaller than or comparable to the symbol size. The models were fit by eye to best match the *IRAS* 60 and 100 μm fluxes.

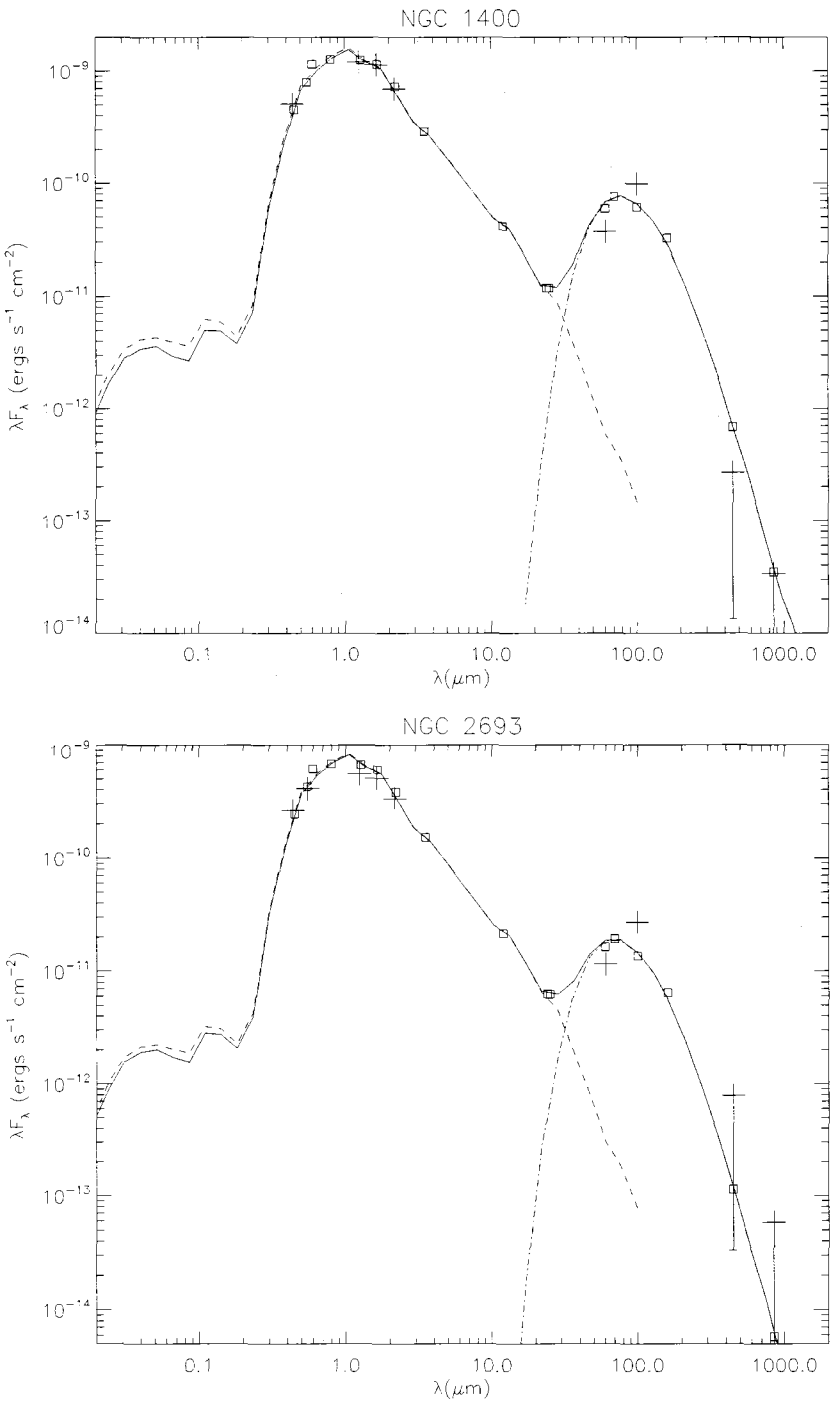

Figure B.1: b.) (*cont'd*) Standard model SEDs.

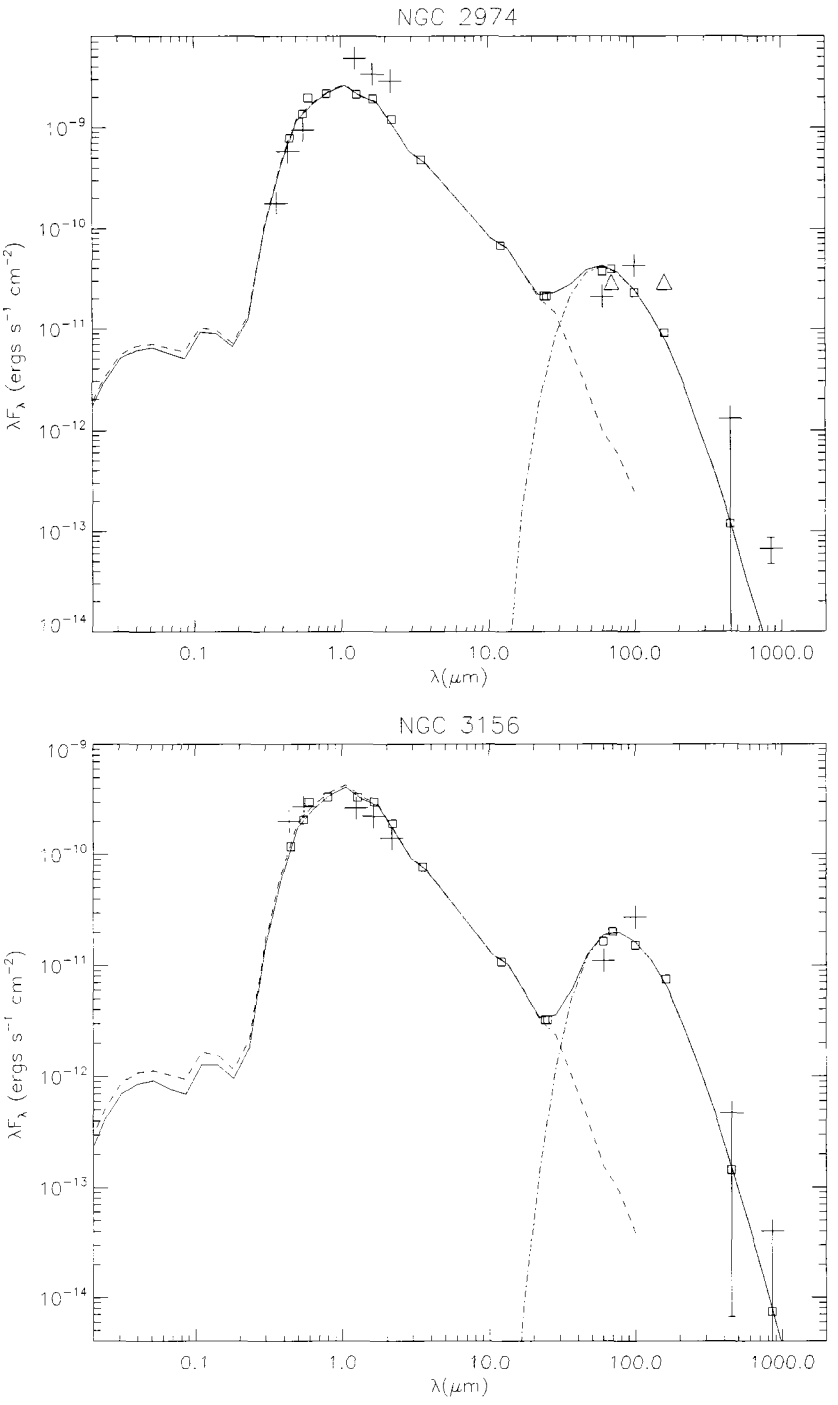

Figure B.1: c.) (*cont'd*) Standard model SEDs.

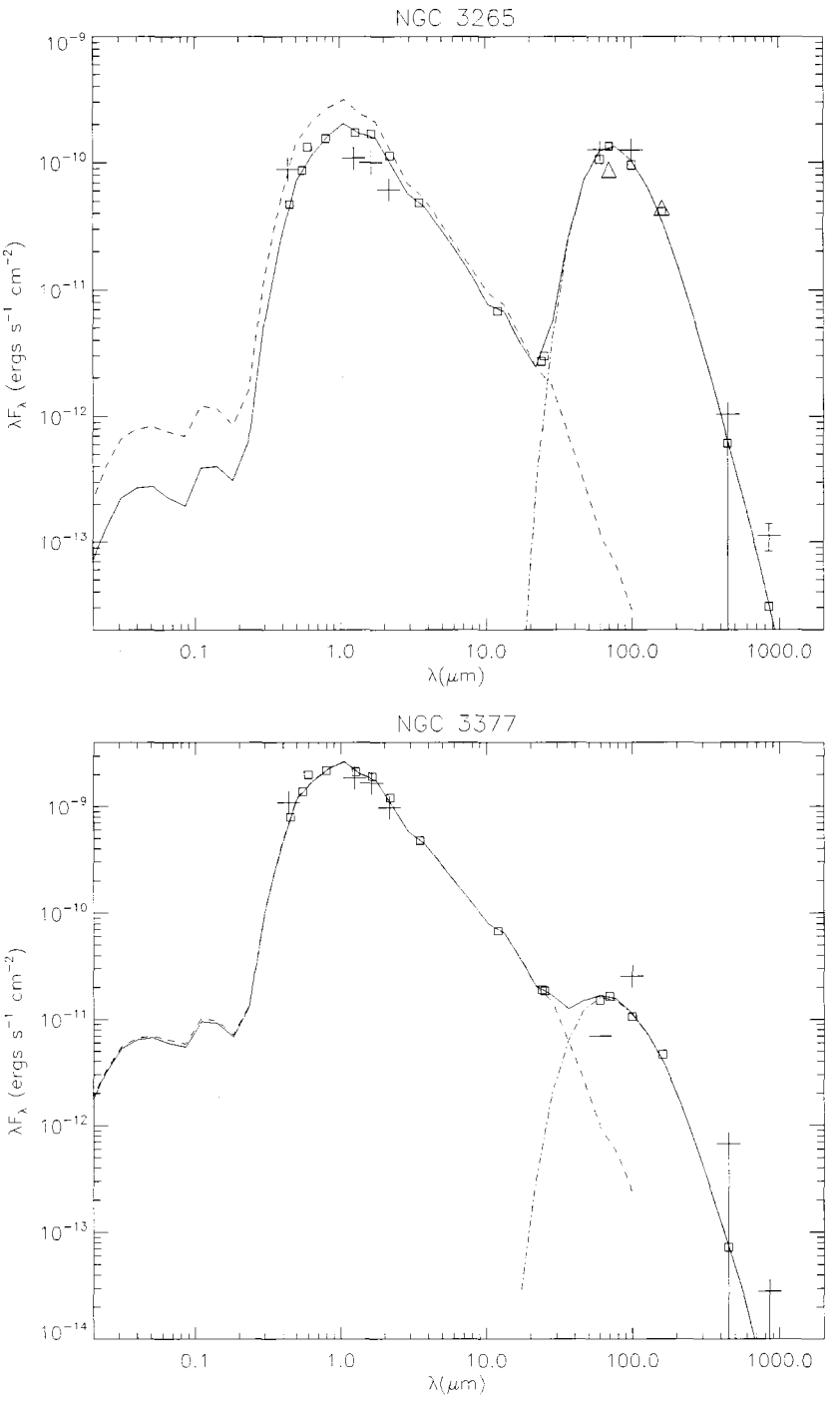

Figure B.1: d.) (*cont'd*) Standard model SEDs.

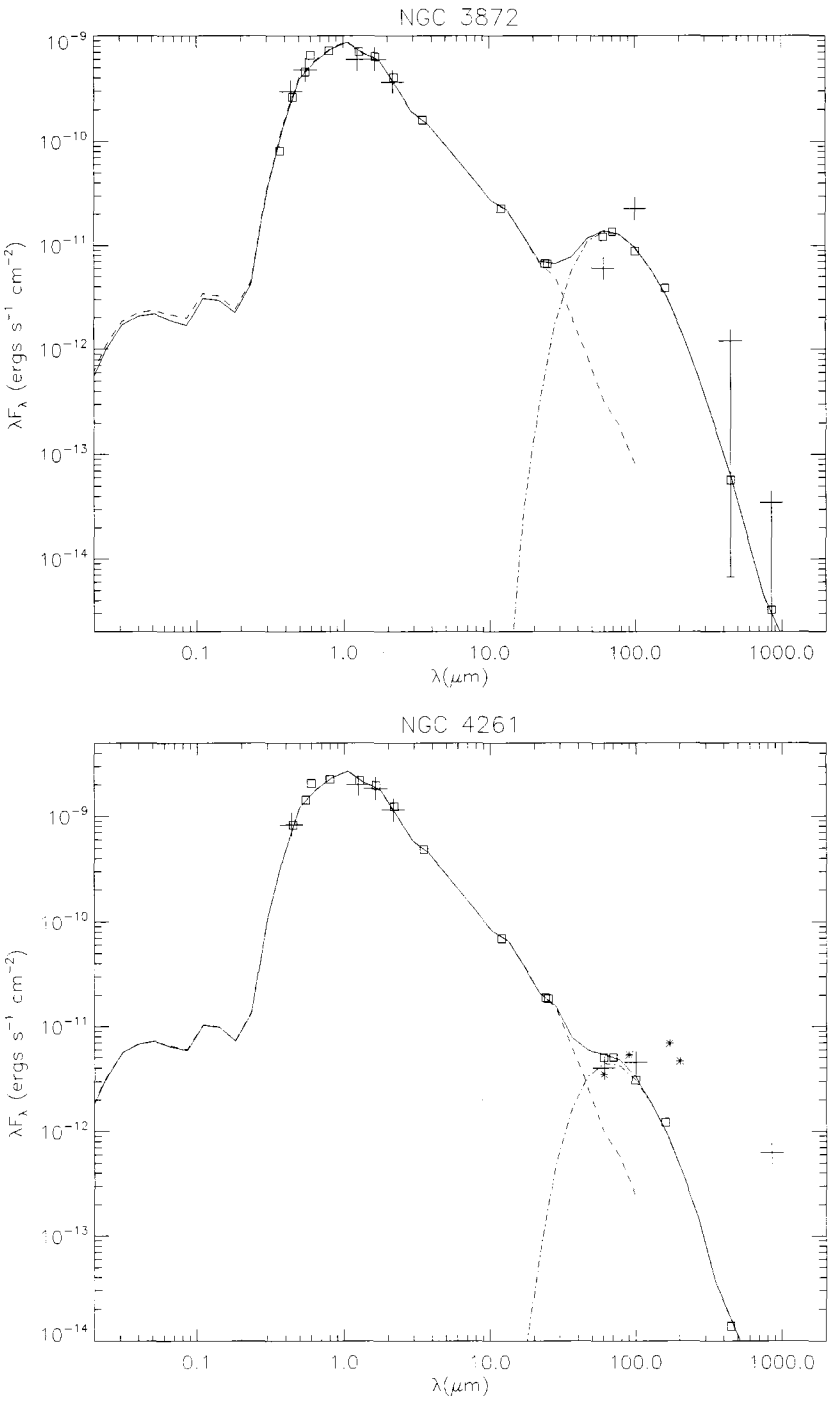

Figure B.1: e.) (*cont'd*) Standard model SEDs.

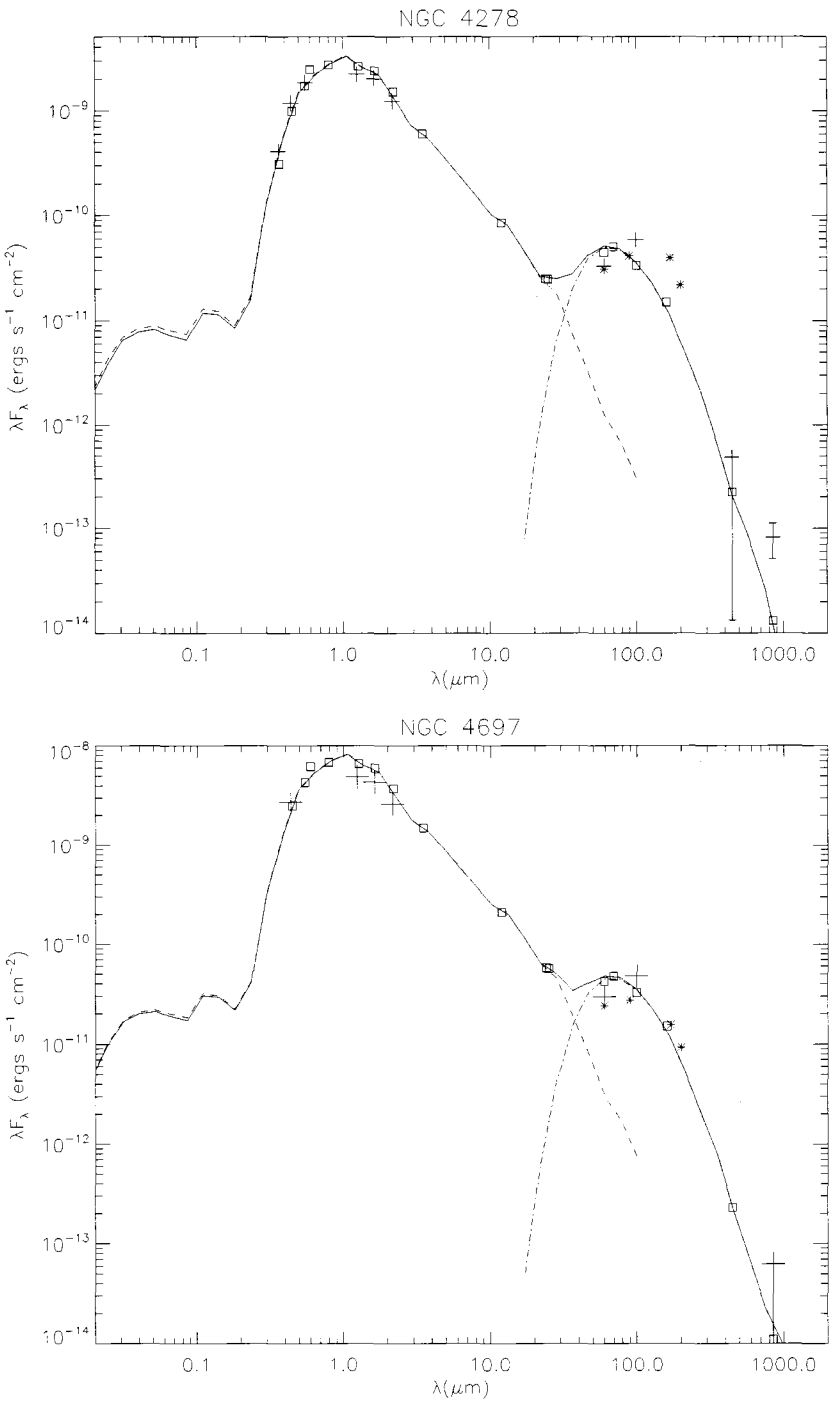

Figure B.1: f.) (*cont'd*) Standard model SEDs.

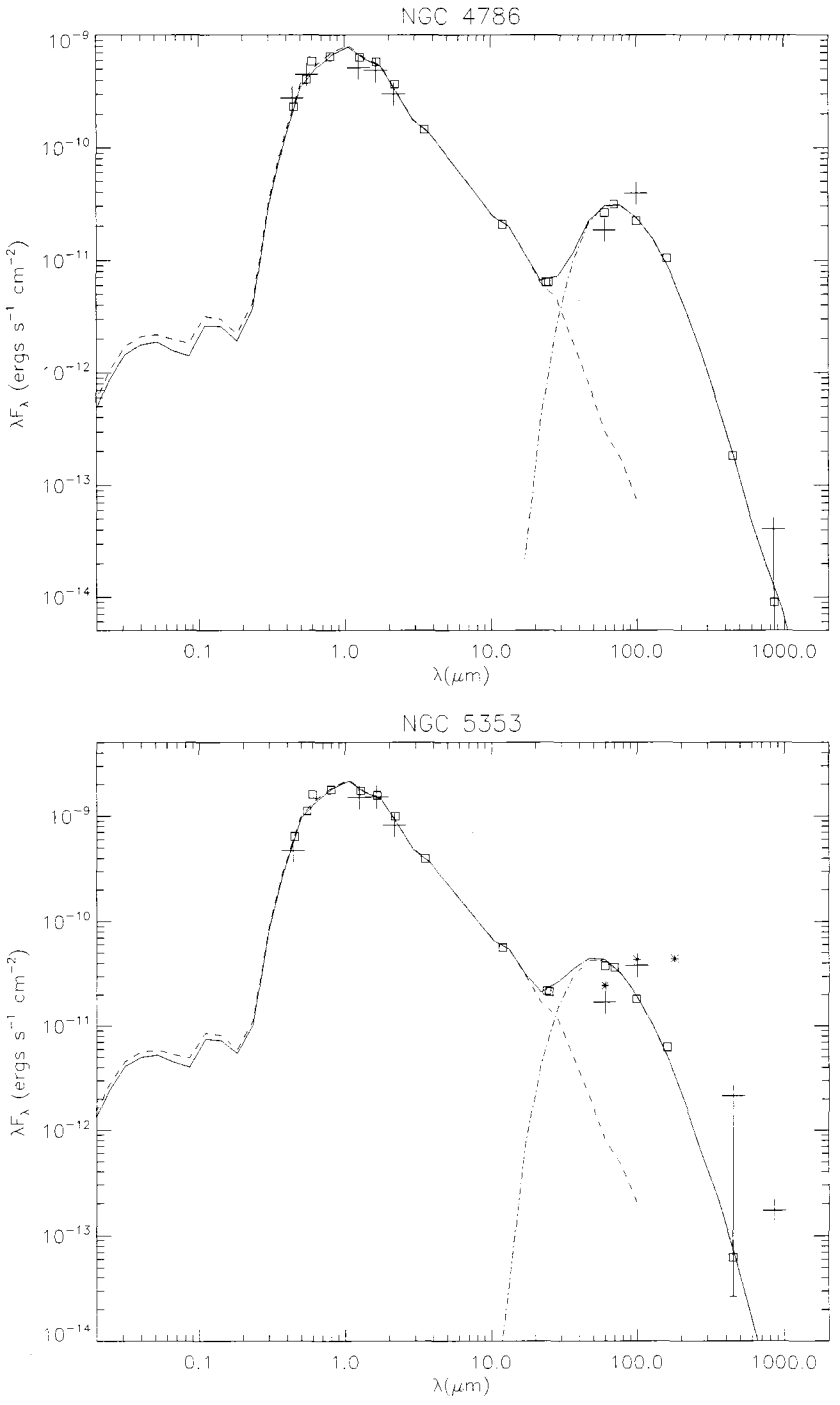

Figure B.1: g.) (*cont'd*) Standard model SEDs.

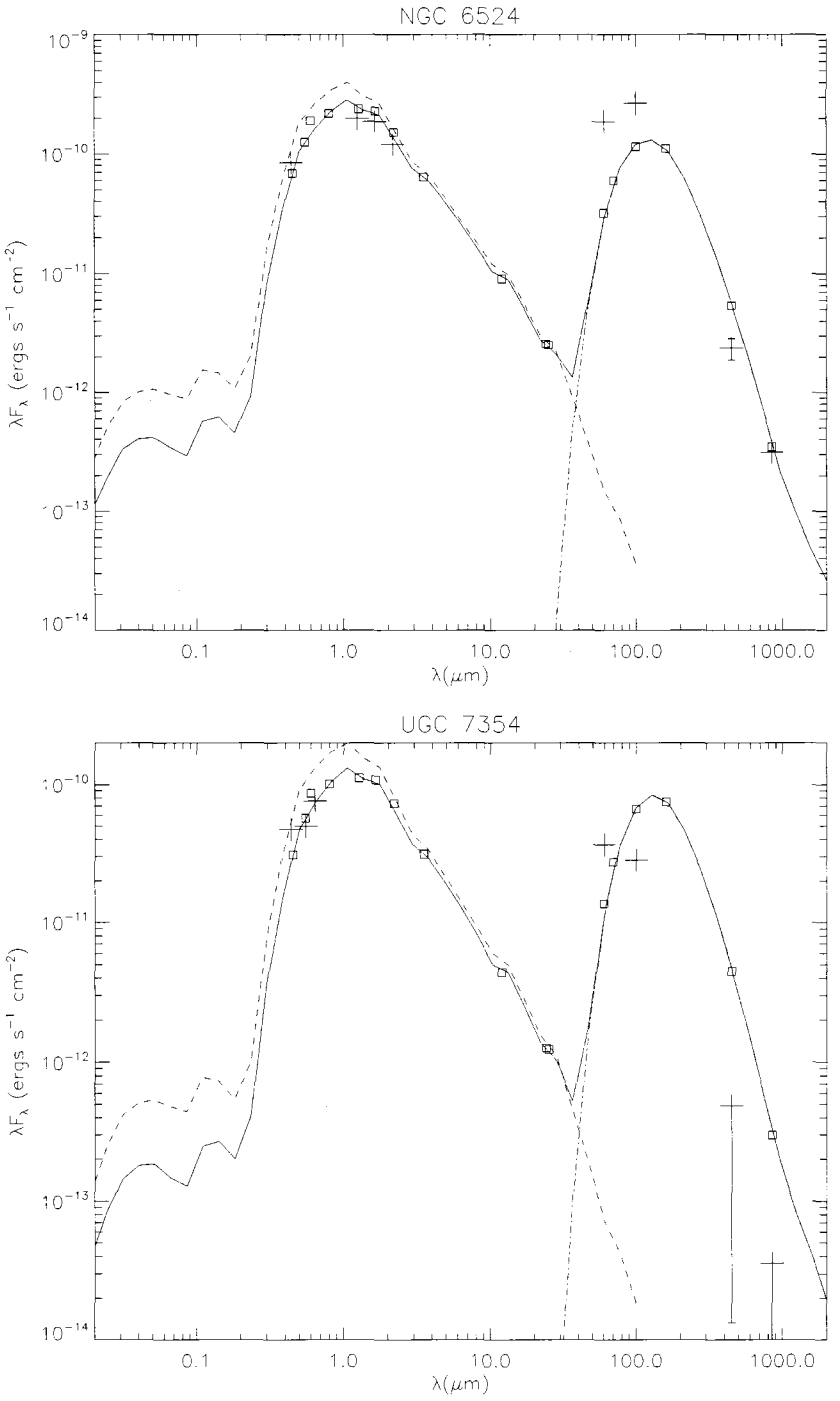

Figure B.1: h.) (*cont'd*) Standard model SEDs.

Bibliography

Athey, A., Bregman, J., Bregman, J., Temi, P., & Sauvage, M. 2002. Mid-Infrared Observation of Mass Loss in Elliptical Galaxies. *ApJ*, **571**(May), 272–281.

Bjorkman, J. E., & Wood, K. 2001. Radiative Equilibrium and Temperature Correction in Monte Carlo Radiation Transfer. *ApJ*, **554**(June), 615–623.

Bregman, J. N., Hogg, D. E., & Roberts, M. S. 1992. Interstellar matter in early-type galaxies. II - The relationship between gaseous components and galaxy types. *ApJ*, **387**(Mar.), 484–502.

Bregman, J. N., Snider, B. A., Grego, L., & Cox, C. V. 1998. Far-Infrared Emission from E and E/S0 Galaxies. *ApJ*, **499**(May), 670–676.

Bruzual A., G., & Charlot, S. 1993. Spectral evolution of stellar populations using isochrone synthesis. *ApJ*, **405**(Mar.), 538–553.

Capaccioli, M., Cappellaro, E., Held, E. V., & Vietri, M. 1993. Deep Kinematics and Dynamics of Edge-On s0 Galaxies - Part One - NGC3115. *A&A*, **274**(July), 69–78.

Carlberg, R. G. 1984. Dissipative formation of an elliptical galaxy. *ApJ*, **286**(Nov.), 403–415.

Carollo, C. M., Danziger, I. J., & Buson, L. 1993. Metallicity Gradients in Early Type Galaxies. *MNRAS*, **265**(Dec.), 553–580.

Ciotti, L., Pellegrini, S., Renzini, A., & D'Ercole, A. 1991. Winds, outflows, and inflows in X-ray elliptical galaxies. *ApJ*, **376**(Aug.), 380–403.

Dale, D. A., Bendo, G. J., Engelbracht, C. W., Gordon, K. D., Regan, M. W., Armus, L., Cannon, J. M., Calzetti, D., Draine, B. T., Helou, G., Joseph, R. D., Kennicutt, R. C., Li, A., Murphy, E. J., Roussel, H., Walter, F., Hanson, H. M., Hollenbach, D. J., Jarrett, T. H., Kewley, L. J., Lamanna, C. A., Leitherer, C., Meyer, M. J., Rieke, G. H., Rieke, M. J., Sheth, K., Smith, J. D. T., & Thornley, M. D. 2005. Infrared Spectral Energy Distributions of Nearby Galaxies. *ApJ*, **633**(Nov.), 857–870.

de Vaucouleurs, G., de Vaucouleurs, A., Corwin, H.G., Buta, R. J., Paturel, G., & Fouque, P. 1991. *Third Reference Catalogue of Bright Galaxies.* Springer-Verlag.

Doi, A., Kameno, S., Kohno, K., Nakanishi, K., & Inoue, M. 2005. A high-frequency radio survey of low-luminosity active galactic nuclei. *MNRAS*, **363**(Oct.), 692–704.

Draine, B. T., & Salpeter, E. E. 1979. On the physics of dust grains in hot gas. *ApJ*, **231**(July), 77–94.

Faber, S. M., & Gallagher, J. S. 1976. H I in early-type galaxies. II - Mass loss and galactic winds. *ApJ*, **204**(Mar.), 365–375.

Fich, M., & Hodge, P. 1991. Continuum emission at 1 millimeter from the elliptical galaxy NGC 205. *ApJL*, **374**(June), L17–L20.

Forman, W., Jones, C., & Tucker, W. 1985. Hot coronae around early-type galaxies. *ApJ*, **293**(June), 102–119.

Freudling, W., Siebenmorgen, R., & Haas, M. 2003. Hot Dust in Radio-loud Active Galactic Nuclei. *ApJL*, **599**(Dec.), L13–L16.

Gallagher, J. S., Faber, S. M., & Balick, B. 1975. H I in early-type galaxies. I - Observations. *ApJ*, **202**(Nov.), 7–21.

Garcia-Burillo, S., Guelin, M., & Cernicharo, J. 1993. CO in M51 - Part One - Molecular Spiral Structure. *A&A*, **274**(July), 123–147.

Gordon, M. A. 1991. Detection of CO emission in the elliptical galaxies NGC 3265 and NGC 5666. *ApJ*, **371**(Apr.), 563–567.

Goudfrooij, P., & de Jong, T. 1995. Interstellar matter in Shapley-Ames elliptical galaxies. IV. A diffusely distributed component of dust and its effect on colour gradients. *A&A*, **298**(June), 784–798.

Hafok, H., & Stutzki, J. 2003. $^{12}CO(J = 2 - 1)$ and $CO(J = 3 - 2)$ observations of Virgo Cluster spiral galaxies with the KOSMA telescope: Global properties. *A&A*, **398**(Feb.), 959–966.

Huchtmeier, W. K., Sage, L. J., & Henkel, C. 1995. Neutral hydrogen observations of elliptical galaxies. II. The IRAS sample. *A&A*, **300**(Aug.), 675–686.

Jaffe, W. 1983. A simple model for the distribution of light in spherical galaxies. *MNRAS*, **202**(Mar.), 995–999.

Jenness, T., Stevens, J. A., Archibald, E. N., Economou, F., Jessop, N. E., & Robson, E. I. 2002. Towards the automated reduction and calibration of SCUBA data from the James Clerk Maxwell Telescope. *MNRAS*, **336**(Oct.), 14–21.

Kaneda, H., Onaka, T., Kitayama, T., Okada, Y., & Sakon, I. 2007. Dust in Hot Plasma of Nearby Dusty Elliptical Galaxies Observed with the Spitzer Space Telescope. *PASJ*, **59**(Feb.), 107–116.

Kim, D.-W. 1989. Interstellar matter in early-type galaxies - Optical observations. *ApJ*, **346**(Nov.), 653–674.

Kim, S.-H., Martin, P. G., & Hendry, P. D. 1994. The size distribution of interstellar dust particles as determined from extinction. *ApJ*, **422**(Feb.), 164–175.

Knapp, G. R., & Rupen, M. P. 1996. Molecular Gas in Elliptical Galaxies: CO Observations of an IRAS Flux-limited Sample. *ApJ*, **460**(Mar.), 271–283.

Knapp, G. R., Kerr, F. J., & Henderson, A. P. 1979. Gas in elliptical galaxies - Limits and detections of 1,000,000-10,000,000 solar masses of H I, and observations of the Coma cluster. *ApJ*, **234**(Dec.), 448–455.

Knapp, G. R., Turner, E. L., & Cunniffe, P. E. 1985. The statistical distribution of the neutral-hydrogen content of elliptical galaxies. *AJ*, **90**(Mar.), 454–468.

Knapp, G. R., Guhathakurta, P., Kim, D.-W., & Jura, M. A. 1989. Interstellar matter in early-type galaxies. I - IRAS flux densities. *ApJS*, **70**(June), 329–387.

Kobayashi, C. 2004. GRAPE-SPH chemodynamical simulation of elliptical galaxies - I. Evolution of metallicity gradients. *MNRAS*, **347**(Jan.), 740–758.

Kobayashi, C., & Arimoto, N. 1999. Gradients of Absorption-Line Strengths in Elliptical Galaxies. *ApJ*, **527**(Dec.), 573–599.

La Barbera, F., de Carvalho, R. R., Gal, R. R., Busarello, G., Merluzzi, P., Capaccioli, M., & Djorgovski, S. G. 2005. Color Gradients in Early-Type Galaxies: Dependence on Environment and Redshift. *ApJL*, **626**(June), L19–L22.

Lauer, T. R., Faber, S. M., Gebhardt, K., Richstone, D., Tremaine, S., Ajhar, E. A., Aller, M. C., Bender, R., Dressler, A., Filippenko, A. V., Green, R., Grillmair, C. J., Ho, L. C., Kormendy, J., Magorrian, J., Pinkney, J., & Siopis, C. 2005. The Centers of Early-Type Galaxies with Hubble Space Telescope. V. New WFPC2 Photometry. *AJ*, **129**(May), 2138–2185.

Mathews, W. G., & Brighenti, F. 2003. Rapid Cooling of Dusty Gas in Elliptical Galaxies. *ApJL*, **590**(June), L5–L8.

Peletier, R. F., Davies, R. L., Illingworth, G. D., Davis, L. E., & Cawson, M. 1990. CCD surface photometry of galaxies with dynamical data. II - UBR photometry of 39 elliptical galaxies. *AJ*, **100**(Oct.), 1091–1142.

Sage, L. J., Welch, G. A., & Young, L. M. 2007. The Cool ISM in Elliptical Galaxies. I. A Survey of Molecular Gas. *ApJ*, **657**(Mar.), 232–240.

Sandell, G., & Weintraub, D. A. 2001. On the Similarity of FU Orionis Stars to Class I Protostars: Evidence from the Submillimeter. *ApJS*, **134**(May), 115–132.

Temi, P., Brighenti, F., Mathews, W. G., & Bregman, J. D. 2004. Cold Dust in Early-Type Galaxies. I. Observations. *ApJS*, **151**(Apr.), 237–269.

Temi, P., Brighenti, F., & Mathews, W. G. 2007. Far-Infrared Spitzer Observations of Elliptical Galaxies: Evidence for Extended Diffuse Dust. *ApJ*, **660**(May), 1215–1231.

Tully, R. B. 1988. *Nearby Galaxies Catalogue.* Cambridge University Press.

Welch, G. A., & Sage, L. J. 2003. The Cool Interstellar Medium in S0 Galaxies. I. A Survey of Molecular Gas. *ApJ*, **584**(Feb.), 260–277.

Wiklind, T., Combes, F., & Henkel, C. 1995. The molecular cloud content of early-type galaxies. V. CO in elliptical galaxies. *A&A*, **297**(May), 643–659.

Wise, M. W., & Silva, D. R. 1996. The Effects of Dust on Broadband Color Gradients in Elliptical Galaxies. *ApJ*, **461**(Apr.), 155–175.

Witt, A. N., Thronson, Jr., H. A., & Capuano, Jr., J. M. 1992. Dust and the transfer of stellar radiation within galaxies. *ApJ*, **393**(July), 611–630.

Wu, H., Shao, Z., Mo, H. J., Xia, X., & Deng, Z. 2005. Optical and Near-Infrared Color Profiles in Nearby Early-Type Galaxies and the Implied Age and Metallicity Gradients. *ApJ*, **622**(Mar.), 244–259.